6

Determination of Speed Parameter

The P-vector inverse method has two steps (a) determination of **P** and (b) determination of the parameter γ (or called the speed parameter). When **P** exists and vertical convergence of diapycnal velocity does not exist, the absolute velocity **V** parallels **P**. Determination of **V** is reduced to the determination of the scalar γ.

6.1 Algebraic Equations

Applying the thermal wind relations (1.4) and (1.5) [or (4.4)] for the z-coordinate (or the isopycnal coordinate) at two different levels z_k and z_m (or ρ_k and ρ_m), a set of algebraic equations for determining the parameter γ are obtained (Chu 1995a)

$$\gamma^{(k)} P_x^{(k)} - \gamma^{(m)} P_x^{(m)} = \Delta u_{km}, \tag{6.1}$$

$$\gamma^{(k)} P_y^{(k)} - \gamma^{(m)} P_y^{(m)} = \Delta v_{km}. \tag{6.2}$$

In the z-coordinate system,

$$\Delta u_{km} \equiv \frac{g}{f\rho_0} \int_{z_m}^{z_k} \frac{\partial \rho}{\partial y} \mathrm{d}z', \Delta v_{km} \equiv -\frac{g}{f\rho_0} \int_{z_m}^{z_k} \frac{\partial \rho}{\partial x} \mathrm{d}z' \tag{6.3}$$

are geostrophic shear at depth z_k relative to z_m. For the isopycnal coordinate system,

$$\Delta u_{km} \equiv \frac{1}{f} \int_{\rho_m}^{\rho_k} \frac{1}{\rho^2} \frac{\partial p}{\partial y} \mathrm{d}\rho, \quad \Delta v_{km} \equiv -\frac{1}{f} \int_{\rho_m}^{\rho_k} \frac{1}{\rho^2} \frac{\partial p}{\partial x} \mathrm{d}\rho \tag{6.4}$$

are geostrophic shear at level ρ_k relative to ρ_m. If the determinant

$$\begin{vmatrix} P_x^{(k)} & P_x^{(m)} \\ P_y^{(k)} & P_y^{(m)} \end{vmatrix} \neq 0, \tag{6.5}$$

the algebraic equations (6.1) and (6.2) have unique solution for $\gamma^{(k)}(m \neq k)$,

$$\gamma^{(k)} = \frac{\begin{vmatrix} \Delta u_{km} & P_x^{(m)} \\ \Delta v_{km} & P_y^{(m)} \end{vmatrix}}{\begin{vmatrix} P_x^{(k)} & P_x^{(m)} \\ P_y^{(k)} & P_y^{(m)} \end{vmatrix}}. \tag{6.6}$$

As soon as $\gamma^{(k)}$ is obtained, the absolute velocity $\mathbf{V}$ is easily computed using (5.3), (5.21), or (5.34). Equation (5.8b) shows that the condition (6.5) is the existence of **P**-spiral. This is to indicate that, for water columns satisfying the two necessary conditions (**P** and **P**-spiral exist) the absolute velocity can be computed.

6.2 Necessary Conditions

Necessary conditions for determination of $\mathbf{V}$ solely from ρ become conditions regarding the vector **P**. The ρ surface does not parallel the q surface, which requires

$$\nabla\rho \times \nabla q \neq 0, \tag{6.7}$$

which leads to the first necessary condition.

Necessary Condition 1: The vector P exists.

Stommel and Scott (1977) pointed out that because the horizontal component of velocity rotates with depth in the open ocean (earlier called the β-spiral), absolute velocities can be obtained from observations of the density field alone. For the set of algebraic equations (6.1) and (6.2) having unique solutions (i.e., the P-vector method works), it requires

$$\sin(\Delta\alpha_{km}) = \begin{vmatrix} P_x^{(k)} & P_x^{(m)} \\ P_y^{(k)} & P_y^{(m)} \end{vmatrix} \neq 0, \tag{6.8}$$

which leads to the second necessary condition.

Necessary Condition 2: The horizontal component of **P** has vertical turning [see (6.8)], or the existence of **P**-spiral (Chu 2000).

Before using any inverse method, these two necessary conditions should be checked. If one of them is not satisfied, no inverse method can be used to obtain the velocity field from the T, S fields for that water column.

6.3 Optimization Scheme

For a given level, $z = z_k$, there are (N–1) sets ($m = 1, 2, k$–$1, k1, \ldots N$) of equations (6.1) and (6.2) for calculating $\gamma^{(k)}$. Here N is the total number of vertical levels of the water column. All the N-1 sets of equations are compatible under the thermal wind constraint and have to provide the same solution. However, because of errors in measurements (instrumentation errors) and computations (truncation errors), the parameter $\gamma^{(k)}$ may vary with m. A least square error algorithm should be used to minimize the error. If the absolute velocity at depth z_m ($u^{(m)}, v^{(m)}$) is known, we may use the thermal wind relation (1.4) and (1.5) to calculate the absolute velocity at any level z_k,

$$\begin{aligned} u^{(k)} &= u^{(m)} + \Delta u_{km}, \quad v^{(k)} = v^{(m)} + \Delta v_{km}, \\ w^{(k)} &= -\frac{u^{(k)}\partial\rho^{(k)}/\partial x + v^{(k)}\partial\rho^{(k)}/\partial y}{\partial\rho^{(k)}/\partial z}. \end{aligned} \tag{6.9}$$

The computed $[u^{(k)}, v^{(k)}, w^{(k)}]$ may not be in the same direction as the vector $\mathbf{P}$ $[P_x^{(k)}, P_y^{(k)}, P_z^{(k)}]$ at the depth z_k. If we assume that the vector $\mathbf{P}$ exists at the depth z_k and that the velocity vector parallels the vector $\mathbf{P}^{(k)}$, an error can be easily defined by (Fig. 6.1)

$$E^{(k)} = \left|\gamma^{(k)}\mathbf{P}^{(k)} - \mathbf{V}^{(k)}\right| = 2\gamma^{(k)} \sin\left[\frac{1}{2}(\theta^{(k)})\right] \cong \gamma^{(k)} \sin\theta^{(k)}, \tag{6.10}$$

where $\theta^{(k)}$ is the angle between $\mathbf{P}^{(k)}$ and $\mathbf{V}^{(k)}$.

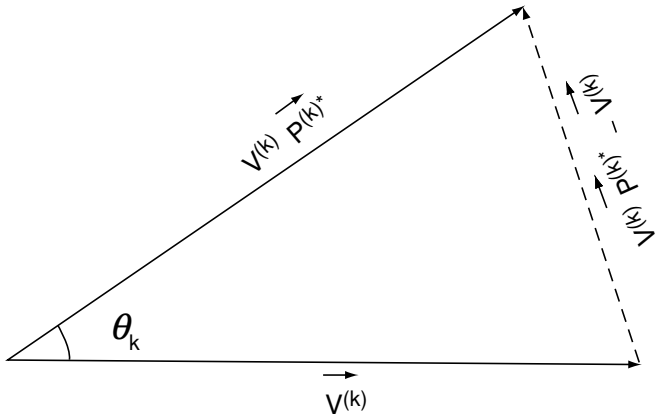

Fig. 6.1. Error at the level k (from Chu et al. 1998d, Journal of Geophysical Research-Oceans)

The total error of the water column velocity caused by the uncertainty of $[u^{(m)}, v^{(m)}]$ is

$$E = \sqrt{\sum_k (h_k E_k)^2}, \tag{6.11}$$

where $h_k = 0.5(z_{k-1} - z_{k+1})$, is the thickness of the layer centered at the kth level. The velocity $[u^{(m)}, v^{(m)}]$ is determined such that the total error E reaches the minimum,

$$\frac{\partial E}{\partial u^{(m)}} = 0, \quad \frac{\partial E}{\partial v^{(m)}} = 0, \tag{6.12}$$

which leads to a 2×2 algebraic equations for determining $[u^{(m)}, v^{(m)}]$,

$$A_{11} u^{(m)} + A_{12} v^{(m)} = F_1, \tag{6.13a}$$

$$A_{21} u^{(m)} + A_{22} v^{(m)} = F_2, \tag{6.13b}$$

where

$$A_{11} = \sum_k a_{11}^{(k)},\ A_{12} = \sum_k a_{12}^{(k)},\ A_{21} = A_{12},\ A_{22} = \sum_k a_{22}^{(k)}, \tag{6.14a}$$

$$F_1 = -\sum_k [a_{11}^{(k)} \Delta u_{km} + a_{12}^{(k)} \Delta v_{km}],\ F_2 = -\sum_k [a_{21}^{(k)} \Delta u_{km} + a_{22}^{(k)} \Delta v_{km}], \tag{6.14b}$$

and

$$a_{11}^{(k)} \equiv [P_y^{(k)}]^2 \chi^{(k)},\ a_{12}^{(k)} = a_{21}^{(k)} \equiv -P_x^{(k)} P_y^{(k)} \chi^{(k)},\ a_{22}^{(k)} \equiv [P_x^{(k)}]^2 \chi^{(k)},$$

$$\chi^{(k)} \equiv \left[1 + \left(\frac{\partial \rho^{(k)}/\partial x}{\partial \rho^{(k)}/\partial z}\right)^2 + \left(\frac{\partial \rho^{(k)}/\partial y}{\partial \rho^{(k)}/\partial z}\right)^2\right] h_k^2. \tag{6.15}$$

If the determinant of (6.13a, b) is nonzero,

$$\begin{vmatrix} A_{11} & A_{12} \\ A_{21} & A_{22} \end{vmatrix} \neq 0, \tag{6.16}$$

the absolute velocity at the level $z = z_m$ can be determined by

$$u^{(m)} = \frac{\begin{vmatrix} F_1 & A_{12} \\ F_2 & A_{22} \end{vmatrix}}{\begin{vmatrix} A_{11} & A_{12} \\ A_{21} & A_{22} \end{vmatrix}}, \quad v^{(m)} = \frac{\begin{vmatrix} A_{11} & F_1 \\ A_{21} & F_2 \end{vmatrix}}{\begin{vmatrix} A_{11} & A_{12} \\ A_{21} & A_{22} \end{vmatrix}}. \tag{6.17}$$

6.4 Evaluation Using the Modular Ocean Model (MOM)

Any inverse method involves two different kinds of errors: observational and modeling errors. The best way to verify the model is to use a no-error data set. Since there is no such data set, we may use a set of steady state solutions from a numerical model as a no-error data set. Chu et al. (1998a) use the steady-state solutions of temperature and salinity from Pacanowski et al. (1991) version of the Modular Ocean Model (MOM), which is based on the work of Bryan (1987).

6.4.1 MOM Implementation

The model domain consists of a $60 \times 65^\circ$ box in latitude-longitude space from 10°N to 70°N and 10°W to 75°W. An idealized shelf with a structure similar to that in Holland (1973) is included along the western boundary. The horizontal grid spacing is 2° latitude by 2° longitude. The model has 12 levels in the vertical, and the depth distribution is listed in Table 6.1.

Values assigned to the various model parameters are listed in Table 6.2. No-slip and insulating boundary conditions are applied at the lateral boundaries. The model uses the Cox (1987) parameterization to compute vertical diffusion and convection implicitly. The enhanced vertical diffusivity in regions of static instability is set at $10\,\mathrm{m^2\,s^{-1}}$. The convective adjustment is used in the model.

The temperature and salinity of upper-most level are eased under a Haney (1971) restoration to a zonally uniform temperature [unit: °C] field,

$$T_a(\varphi) = 30.0 - \frac{33.0}{80.0}\varphi + 40.0 \sin\left[\frac{2\pi}{75.0}(\varphi - 5.0)\right], \tag{6.18}$$

Table 6.1. Vertical levels for MOM modeling

k	z-level (m)	k	z-level (m)
1	−12.5	7	−635.0
2	−37.5	8	−1,025.0
3	−70.0	9	−1,575.0
4	−125.0	10	−2,350.0
5	−215.0	11	−3,250.0
6	−370.0	12	−4,150.0

Table 6.2. MOM parameters

parameter	symbol	value
horizontal diffusivity	A_{TH}	$1 \times 10^3\,\mathrm{m^2\,s^{-1}}$
horizontal viscosity	A_{MH}	$2 \times 10^5\,\mathrm{m^2\,s^{-1}}$
vertical diffusivity	A_{TV}	$1 \times 10^{-4}\,\mathrm{m^2\,s^{-1}}$
vertical viscosity	A_{MV}	$1 \times 10^{-4}\,\mathrm{m^2\,s^{-1}}$
characteristic density	P_0	$1,025\,\mathrm{kg\,m^{-3}}$
heat capacity	C_w	$4 \times 10^3\,\mathrm{J\,kg^{-1}\,K^{-1}}$

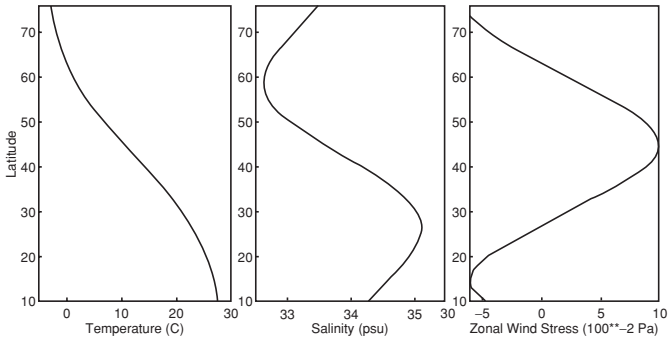

Fig. 6.2. Surface boundary conditions. Temperature and salinity fields used in the Haney-type restoring forcing condition and the surface wind stress (from Chu et al. 1998a, Journal of Oceanography)

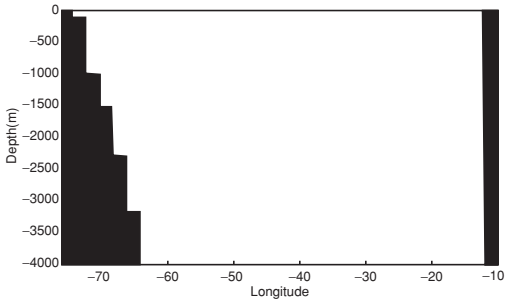

Fig. 6.3. The x-dependent bottom topography used in the MOM model (from Chu et al. 1998a, Journal of Oceanography)

and a salinity [unit: ppt] field

$$S(\varphi) = 35.0 - \frac{1.32}{50.0}\varphi + 0.84 \sin\left[\frac{2\pi}{55.0}(\varphi - 15.0)\right], \tag{6.19}$$

with relaxation time-scale of 25 days (over a modeled top mixed 25 m). Figure 6.2 shows the surface boundary conditions and the zonal wind stress. The bottom topography is assumed to be only dependent on x, and has a staircase-type change west of 64°W and no change east of 64°W (Fig. 6.3).

The techniques of Bryan (1987) for acceleration equilibration of the model solution are used. This includes using a longer time-step at any depth. The acceleration factor increases from one at the surface level to eight at the bottom level. After 750 surface years (6,000 years at the bottom) the model reaches a statistically steady state (total kinetic energy reaches equilibrium).

6.4.2 MOM Generated Steady-State (ρ, q) Data

The MOM model output includes potential temperature, salinity, and velocity $(u,\ v,\ w)$. The statistically steady potential density field (ρ) is computed from the temperature and salinity fields. Figure 6.4 shows the $\sigma_\theta(\equiv \rho - 1,000)$ field at different depths. The most evident features are listed as follows. The maximum values (29.2–29.3 $\mathrm{kg\,m^{-3}}$) appear at the high latitudes (near 70°N) at all depths. The horizontal σ_θ gradient reduces as the depths increases. The low σ_θ water appears at the equatorial region near surface and stretches northward as the depth increases. Near the surface (Fig. 6.4a) the σ_θ contours are almost zonal except at the western boundary, where the σ_θ contours bend towards the north, indicating the northward movement of low σ_θ equatorial water. At the depths of 37.5 m (Fig. 6.4b) and 70 m (Fig. 6.4c), the northward movement of the equatorial low σ_θ water becomes more evident. At the depth of 215 m (Fig. 6.4d), the low σ_θ zone shifts northward. Two centers of low σ_θ (27.4 $\mathrm{kg\,m^{-3}}$) are found at the southwest corner (25°N, 74°W) and at the middle of the eastern boundary. At the deep levels (Figs. 6.4e and 6.4f), σ_θ is very uniform. The minimum zone of σ_θ is located at around 60°N.

The statistically steady potential vorticity field (q) is computed from σ_θ. Figure 6.5 shows the $q(=f\partial\rho/\partial z)$ field at different depths. The most evident features are listed as follows. The values of q are either negative or zero. There is an anticyclonic gyre occupying the majority of the domain. In upper levels (12.5 m, 37.5 m, and 70 m), the strongest negative q center (with a value around $-1.4 \times 10^{-6}\,\mathrm{kg\,m^{-4}\,s^{-1}}$) is located near the southwest corner (60°–70°W, 20°–35°N). As depth increases, the magnitude of q-values reduces. The strongest negative q center, with values around $-2.5 \times 10^{-8}\,\mathrm{kg\,m^{-4}\,s^{-1}}$ at 1,575 m depth and $-2.2 \times 10^{-9}\,\mathrm{kg\,m^{-4}\,s^{-1}}$ at 3,250 m depth (2–3 orders of magnitude smaller than the upper levels), is located near the northeast corner (20°–10°W, 55°–65°N).

6.4.3 MOM Generated Statistically Steady-State Velocity Field

Figure 6.6 shows the MOM generated statistically steady horizontal velocities at several depths (a) 12.5 m, (b) 37.5 m, (c) 70 m, (d) 215 m, (e) 1,575 m, and (f) 3,250 m. The circulation patterns can be outlined as follows. Westward-moving equatorial currents are evident in upper levels ($z \geq -215$ m) and disappear in the deeper layer ($z < -215$ m). The width of the upper layer equatorial current is around 6° in latitude.

When the upper layer equatorial current approaches the western boundary, it turns direction and becomes the western boundary current. The maximum velocity of the western boundary current reaches 13 $\mathrm{cm\,s^{-1}}$. The intermediate level (1,575 m) and deep level (3,250 m) feature a westward current originating at the northeast corner. This current turns southwestward at around 50°W and branches into two western boundary currents (northward and southward)

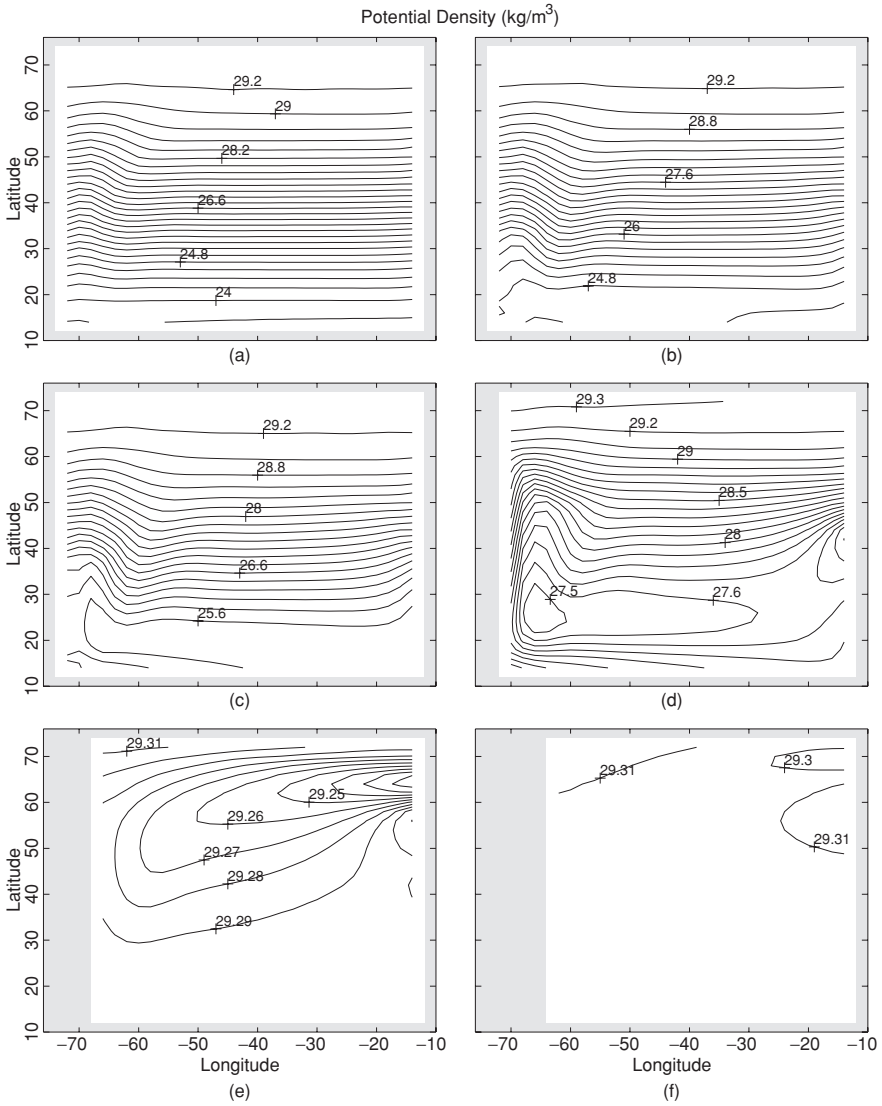

Fig. 6.4. Statistically steady potential density ($\mathrm{kg\,m^{-3}}$) from the MOM simulation at different depths (**a**) 12.5 m, (**b**) 37.5 m, (**c**) 70 m, (**d**) 215 m, (**e**) 1,575 m, and (**f**) 3,250 m (from Chu et al. 1998a, Journal of Oceanography)

while approaching the western boundary. The bifurcation is found at 40°N for the depth of 1,575 m, and at 60°N for the depth of 3,250 m. The deep currents are weak ($\leq 2\,\mathrm{cm\,s^{-1}}$).

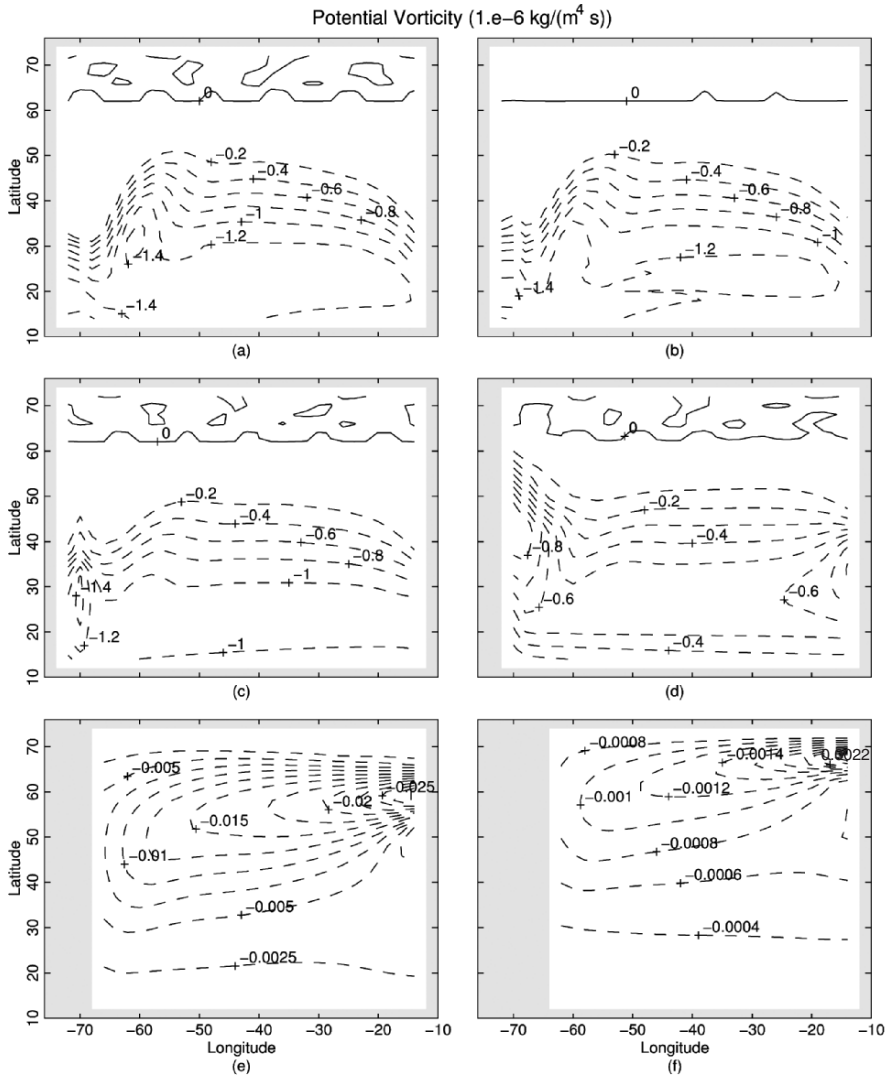

Fig. 6.5. Statistically steady potential vorticity (in $10^{-6}\,\mathrm{kg\,m^{-4}\,s^{-1}}$) from the MOM simulation at different depths (**a**) 12.5 m, (**b**) 37.5 m, (**c**) 70 m, (**d**) 215 m, (**e**) 1,575 m, and (**f**) 3,250 m (from Chu et al. 1998a, Journal of Oceanography)

6.4.4 Necessary Condition Check-up

Before testing the P-vector method, the MOM (ρ, q) data are checked if the two necessary conditions are satisfied. The vector product of $\nabla\rho$ and ∇q is given by

$$\nabla\rho \times \nabla q = \mathbf{P}\,|\nabla\rho|\,|\nabla q|\sin\delta, \tag{6.20}$$

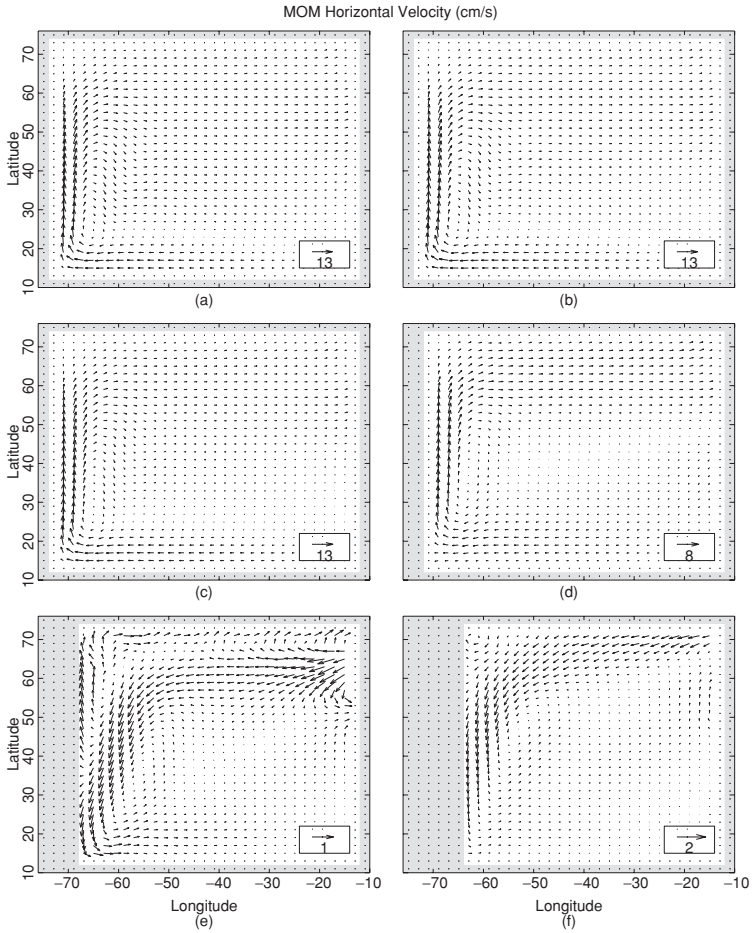

Fig. 6.6. Statistically steady horizontal velocity vector (in $\mathrm{cm\,s^{-1}}$) from the MOM simulation at different depths (**a**) 12.5 m, (**b**) 37.5 m, (**c**) 70 m, (**d**) 215 m, (**e**) 1,575 m, and (**f**) 3,250 m (from Chu et al. 1998a, Journal of Oceanography)

where δ is the intersection angle between $\nabla\rho$ and ∇q. Since δ cannot be exactly zero when computed from data. A small value (10^{-5}) is taken as the criterion, if $|\sin\delta| \leq 10^{-5}$, the ρ surface is thought to be parallel to the q surface. Figure 6.7 shows the regions at six different depths where the first necessary condition fails.

The velocity spiral from the MOM simulation can be identified for each grid point by the plot of the horizontal velocity of all depths (Fig. 6.8). There are 12 vectors at each grid. Coincidence of the vectors indicates that there is no vertical turning. Two numbers given at each grid indicate the maximum turning between two consecutive levels such as from 370-m (level 6) to 635-m (level 7) in the subtropical regions (10°–30°N) and from 1,025-m (level 8)

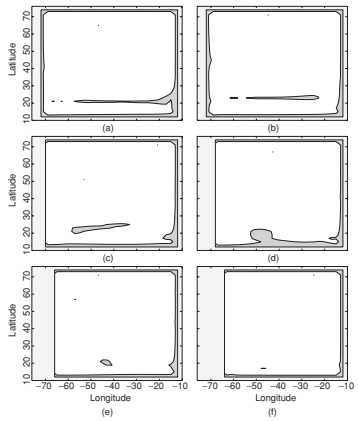

Fig. 6.7. Regions with $|\sin\delta| \leq 10^{-5}$ at different depths (**a**) 12.5 m, (**b**) 37.5 m, (**c**) 70 m, (**d**) 215 m, (**e**) 1,575 m, and (**f**) 3,250 m (from Chu et al. 1998a, Journal of Oceanography).

to 1,575-m (level 9) in the mid- and high- latitudes (north of 40°N) regions. At some locations, the maximum turning occurs at deeper levels. Usually, strong vertical turning of the horizontal velocity indicates a strong baroclinicity. This also implies that the second necessary condition (existence of spiral) is satisfied.

6.4.5 Absolute Velocities Obtained from the P-Vector Inverse Method Using MOM T, S Output

Taking the statistically steady potential temperature and salinity fields as no-error data sets, we employed the P-vector inverse method to obtain the 3-D absolute velocity (u, v). Figure 6.9 shows the vector plots of the horizontal velocities at several different depths (a) 12.5 m, (b) 37.5 m, (c) 70 m, (d) 215 m, (e) 1,575 m, and (f) 3,250 m. The circulation patterns are very similar to the MOM statistically steady-state velocity fields in the upper four levels (12.5 m, 37.5 m, 70 m, and 215 m). The circulation patterns can be outlined as follows. Westward-moving equatorial currents are evident with a width of 6° in latitude. When the equatorial current approaches the western boundary, it turns direction and become the western boundary current. The current velocities are similar at the three levels: 12.5 m, 37.5 m, and 70 m, but weaker in the P-vector inverse method. The lower level (1,575 and 3,250 m) velocity fields are very weak. The major difference between the MOM and the inverse solutions is the western boundary flow bifurcation. The MOM model shows the high latitude westward flow bifurcated at 40°N for the depth of 1,575 m, and at 60°N for the depth of 3,250 m into two western boundary currents (northward and southward). However, the P-vector inverse model does not show this bifurcation.

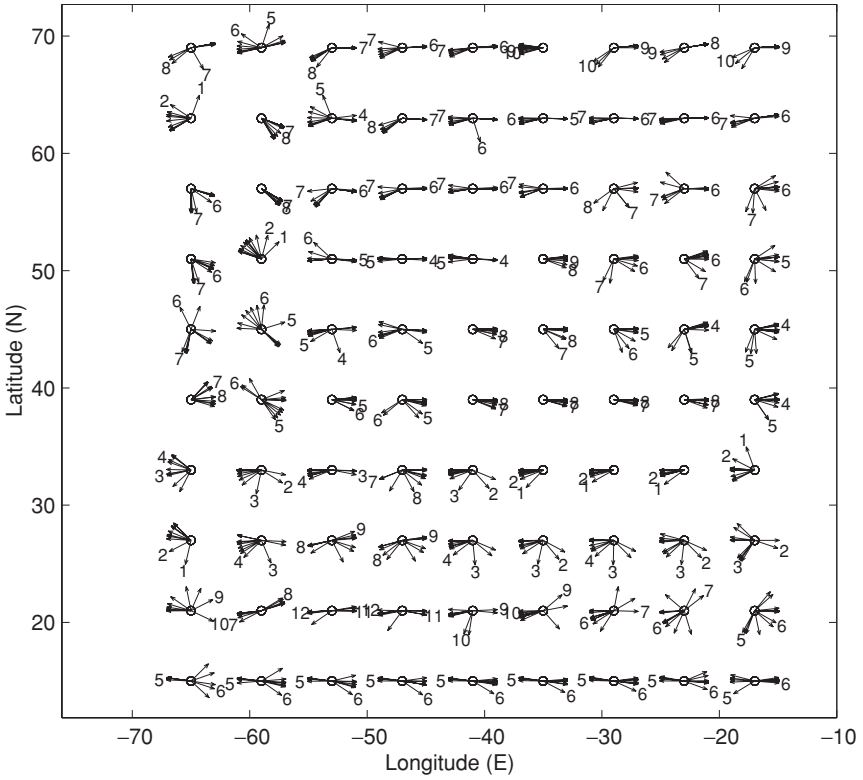

Fig. 6.8. P-Spirals of the horizontal velocity (12 vectors at each grid). Two numbers given at each grid indicate the maximum turning between two consecutive levels (from Chu et al. 1998a, Journal of Oceanography)

6.4.6 Comparison between Nondivergent Portions of Two Flow Fields

Given that the MOM model flow field derives from primitive equation dynamics, we do not expect that the velocity fields from the P-vector method (assuming geostrophic dynamics) match the MOM model velocity fields. The only valid comparison should be with the nondivergent portion of the flow field,

$$\nabla^2 \Psi_{\mathrm{MOM}} = \frac{\partial (f v_{\mathrm{MOM}})}{\partial x} - \frac{\partial (f u_{\mathrm{MOM}})}{\partial y}, \tag{6.21}$$

$$\nabla^2 \Psi = \frac{\partial (f v)}{\partial x} - \frac{\partial (f u)}{\partial y}, \tag{6.22}$$

which are solved by taking (u_{MOM}, v_{MOM}), (u, v) as forcing functions under the boundary conditions

$$\Psi_{\mathrm{MOM}}|_{\Gamma} = 0, \quad \Psi|_{\Gamma} = 0, \tag{6.23}$$

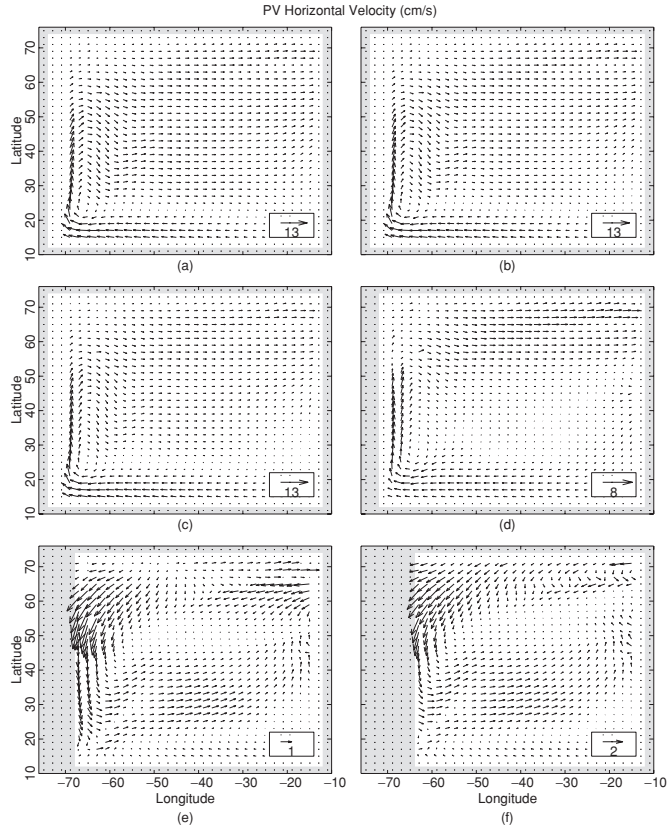

Fig. 6.9. Absolute velocity fields computed using the P-vector method at different depths (**a**) 12.5 m, (**b**) 37.5 m, (**c**) 70 m, (**d**) 215 m, (**e**) 1,575 m, and (**f**) 3,250 m (from Chu et al. 1998a, Journal of Oceanography)

where Γ represents the lateral boundaries. The Ψ_{MOM} field has the following features (Fig. 6.9): a nearly basin-wide anticyclonic gyre in the upper levels (12.5 m, 37.5 m, 70 m, and 215 m) and a nearly basin-wide cyclonic gyre in the lower levels (1,575 m, 3,250 m).

These gyres are evident by closed Ψ_{MOM} contours with a maximum value for the anticyclonic gyre and with a minimum value for the cyclonic gyre. Both basin-wide gyres are asymmetric. The center of the gyres (both upper and lower levels) is towards the west, with a strong western boundary current. In the upper levels, a weak and narrow cyclonic gyre appears in the high latitudes (north of 60°N) east of 55°W (south of Greenland and Iceland.) This weak high latitude cyclonic gyre reduces its size with depth and becomes an anticyclonic gyre which stretches westward to the western boundary in the intermediate level (1,575 m). In the deep level (3,250 m), the cyclonic gyre fills the whole basin.

The streamfunction Ψ (Fig. 6.9) at the six different depths shows that the pattern of the two fields are quite similar: a nearly basin-wide anticyclonic gyre in the upper levels (12.5 m, 37.5 m, 70 m, and 215 m) and a nearly basin-wide cyclonic gyre in the lower levels (1,575 m, 3,250 m). These gyres are featured by closed Ψ contours with a maximum value for the anticyclonic gyre and a minimum value for the cyclonic gyre. The center of the basin-wide gyres (both upper and lower levels) is towards the west, and has a strong western boundary current. The patterns are very similar between $\Psi_{\rm MOM}$ and Ψ at all depths.

The differences between $\Psi_{\rm MOM}$ and Ψ are (a) the nearly basin-wide gyre is stronger in the MOM model than in this P-vector model except for the intermediate level (1,575 m), where the cyclonic gyre obtained by the P-vector method is stronger; (b) in the upper levels (12.5 m, 37.5 m, 70 m, and 215 m) the high latitude (north of 60°N) cyclonic gyre obtained by the P-vector model stretches from the eastern boundary to the western boundary; and (c) in the intermediate level (1,575 m), the high latitude anticyclonic gyre by the P-vector model is located in the eastern part (east of 40°W) rather than stretching to the western boundary in the MOM model.

Relative difference (I_Ψ) between $\Psi_{\rm MOM}$ and Ψ for each level can be depicted by a ratio between root-mean-square difference and standard deviation of MOM results ($\mathrm{dev}_{\Psi_{\rm MOM}}$),

$$I_\Psi = \frac{\sqrt{\frac{1}{M-1}\sum(\Psi_{\rm MOM}-\Psi)^2}}{\sigma_{\Psi_{\rm MOM}}}, \tag{6.24}$$

$$\mathrm{dev}_{\Psi_{\rm MOM}} = \sqrt{\frac{1}{M-1}\sum(\Psi_{\rm MOM}-\bar{\Psi}_{\rm MOM})^2}, \tag{6.25}$$

where M is the total number of the horizontal grid points, and $\bar{\Psi}_{\rm MOM}$ is the horizontal mean. The numerator and denominator of (6.24) show the mean difference between two streamfunctions and the variability of $\Psi_{\rm MOM}$. The smaller the I_Ψ, the smaller is the difference between the inverse and MOM solutions. Near the surface, I_Ψ is small ($\sim$0.15), increases with depth until 1,000 m (level eight) with the maximum value of 0.8, and then decreases with depth (Fig. 6.10). In deep levels ($z \le -2{,}500$ m), I_Ψ reduces with depth from 0.3 to 0.2. Near the bottom, I_Ψ is around 0.2. The maximum value of I_Ψ may be caused by strong baroclinicity near that level (Fig. 6.10).

6.5 z-Coordinate System

In this section, the Japan/East Sea is used as an example to illustrate the ordinary P-vector inverse method in the z-coordinate system (Chu 1995a; Chu et al. 2001a).

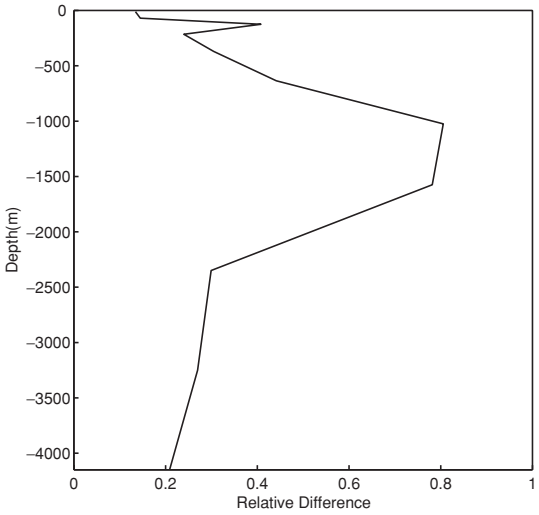

Fig. 6.10. Vertical variation of the relative difference I_Ψ (from Chu et al. 1998a, Journal of Oceanography)

6.5.1 Japan/East Sea

The Japan Sea, known as the East Sea in Korea, has steep bottom topography (Fig. 6.11) that makes it a unique semienclosed ocean basin overlaid by a pronounced monsoon surface wind. The Japan Sea covers an area of $10^6\,\mathrm{km}^2$, has a maximum depth in excess of 3,700 m, and is isolated from open oceans except for small (narrow and shallow) straits which connect the Japan Sea to the Pacific Ocean.

The Japan/East Sea contains three major basins called the Japan Basin, Ulleng/Tsushima Basin, and Yamato Basin, and a high central seamount called the Yamato Rise. The Japan Sea is of a great scientific interest as it is taken as a miniature prototype of the ocean. Its basin-wide circulation pattern, boundary currents, Subpolar Front, mesoscale eddy activities, and deep water formation are similar to those in a large ocean. It experiences two monsoons, winter and summer, every year. During the winter monsoon season, a cold northwest wind blows over the Japan Sea as a result of the Siberian High Pressure System located over the East Asian continent. Radiative cooling and persistent cold air advection maintain cold air over the Japan/East Sea. The northwest-southeast oriented Jet Stream is positioned above it. Such a typical winter monsoon pattern lasts nearly six months (November–April). During the summer monsoon, a warm and weaker southeast wind blows over

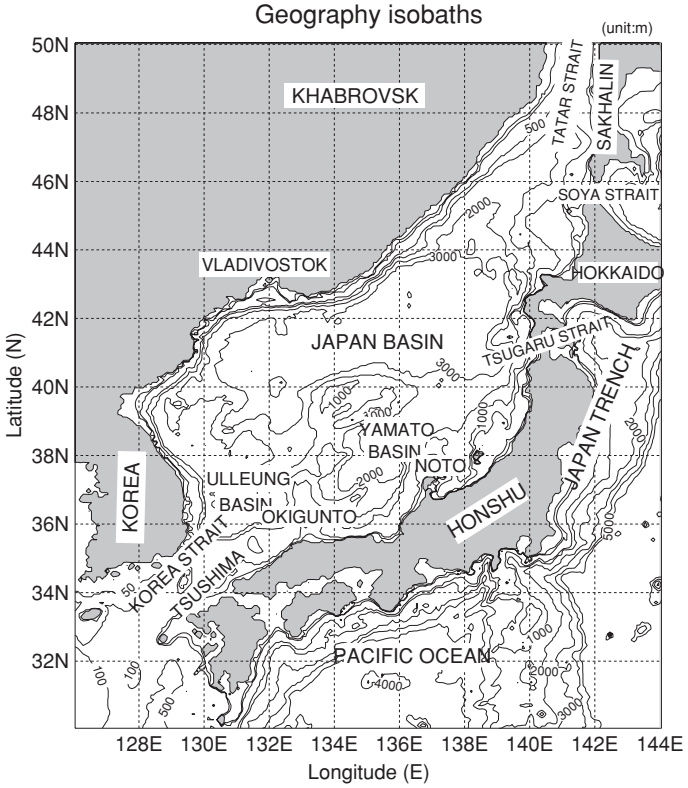

Fig. 6.11. Geography and isobaths showing the bottom topography (in meters) of the Japan/East Sea (from Chu et al. 2001a, Journal of Physical Oceanography)

the Japan/East Sea. Such a typical summer monsoon pattern lasts nearly four months (mid-May to mid-September).

The Japan/East Sea thermohaline structure and general circulation have been investigated for several decades. The Tsushima Warm Current (Mitta and Ogawa 1984), dominating the surface layer, flows in from the Tsushima Strait, and carries warm water from the south up to 40°N where a polar front forms (Seung and Yoon 1995). Most of the nearly homogeneous water in the deep part of the basin is called the Japan Sea Proper Water (Moriyasu 1972) and is of low temperature and low salinity. Above the Proper Water, warm and saline water flows in through the Tsushima Strait, transports northeastward, and flows out through the Tsugaru and Soya Strait.

The Tsushima Warm Current separates north of 35°N into western and eastern channels (Uda 1934; Kawabe 1982a,b; Hase et al. 1999; Senjyu 1999). The flow through the western channel closely follows the Korean coast (called the East Korean Warm Current) until it bifurcates into two branches near 37°N. The eastern branch follows the Subpolar Front to the western coast

of Hokkaido Island, and the western branch moves northward and forms a cyclonic eddy at the Eastern Korean Bay. The flow through the eastern channel follows the Japanese coast, called the Near-shore Branch by Yoon (1982). More accurately, we may call it the Japan Near-shore Branch, which is usually weaker than the East Korean Warm Current. The Tsushima Warm Current at both channels reduces with depth. The East Korean Warm Current meets the southward coastal current, the North Korean Cold Current, at about 38°N with some seasonal meridional migration. After separation from the coast, the East Korean Warm Current and the North Korean Cold Current converge and form a strong front (i.e., the Subpolar Front) that stretches in a west-east direction across the basin. The North Korean Cold Current makes a cyclonic recirculation gyre in the north but most of the East Korean Warm Current flows out through the outlets (Uda 1934). The formation of the North Korean Cold Current and the separation of the East Korean Warm Current are due to a local forcing by wind and buoyancy flux (Seung 1992). Large meanders develop along the front and are associated with warm and cold eddies.

Between the Tsushima Warm Current water and the Japan Sea Proper Water, a vertical salinity minimum south of the Subpolar Front, usually accompanied by the dissolved oxygen maximum, was first found and named the Japan Sea Intermediate Water by Miyazaki (1952, 1953), and further depicted by Kajiura et al. (1958) and Moriyasu (1972). The colocation of the salinity minimum and the dissolved oxygen maximum implies that the Intermediate Water originates from the descending surface water around the Subpolar Front (Miyasaki 1952, 1953; Miyasaki and Abe 1960). Later, Kim and Chung (1984) found very similar property in the Ulleung/Tsushima Basin and proposed the East Sea Intermediate Water (i.e., Japan Sea Intermediate Water used by the Japanese oceanographers); and Kim and Kim (1999) found the high salinity water with high oxygen in the eastern Japan Basin (i.e., north of Subpolar Front) and named the water the High Salinity Intermediate Water ($S > 34.07$ ppt).

The seasonal variability of both the Japan Sea circulation and thermohaline structure has been studied based on limited datasets such as the seasonal SST variability (Isoda and Saitoh 1988, 1993; Kano 1980; Maizuru Marine Observatory 1997). Based on the satellite infrared images in the western part of the Japan Sea and the routine hydrographic survey by the Korea Fisheries Research and Development Agency in 1987, Isoda and Saitoh (1993) found SST patterns in winter and spring which are characterized as follows: A small meander of a thermal front was first originated from the Tsushima Strait near the Korean coast and gradually grew into an isolated warm eddy with a horizontal scale of 100 km. The warm eddy intruded slowly northward from spring to summer. Chu et al. (1998a) reported the seasonal occurrence of Japan Sea eddies from the composite analysis on the U.S. National Centers for Environmental Prediction (NCEP) monthly SST fields (1981–1994). For example, they identified a warm center appearing in later spring in the East Korean Bay. Recently, Park and Chu (2006a) investigate the interannual SST

variability from the reconstructed NOAA/AVHRR Oceans Pathfinder best SST data (1985∼2002) using the complex empirical function (CEOF) analysis. The first CEOF mode represents a standing oscillation and a maximum belt in the central Japan/East Sea. There are two near 7-year events and one 2–3-year event during the period of 1985–2002. The first mode oscillates by adjacent atmospheric systems such as the Aleutian Low, the North Pacific High, the Siberian High, and the East Asian jet stream. Positive correlation in a zonal belt between the first mode SST anomaly and the background surface air temperature/SST anomaly shows the intensive ocean–atmosphere interaction near the Polar Front in the North Pacific.

6.5.2 GDEM for the Japan/East Sea

Data for building the current version of GDEM climatology for the Japan Sea were obtained from the MOODS, which has 136,509 temperature and 52,572 salinity profiles during 1930–1997. The main limitation of the MOODS data is its irregular distribution in time and space. Certain periods and areas are over sampled while others lack enough observations to gain any meaningful insights. Vertical resolution and data quality are also highly variable depending much on instrument type and sampling expertise (Chu et al. 1997a–d). The monthly distributions of the Japan Sea temperature (Fig. 6.12a) and salinity (Fig. 6.12b) stations show that the number of temperature stations is 2–3 times more than the number of salinity stations. January has the least profiles while August has the most.

The seasonal T, S variation reduces as the depth increases. At 300-m depth there is almost no seasonal variability. Thus, we only present the horizontal fields at the surface and the intermediate level (150-m) for illustration. In order to see the seasonal variation of the vertical thermohaline structure, we present the latitudinal and zonal cross-sections of the monthly mean fields. To identify the variability in both monthly-mean and monthly-mean anomaly fields, we use a cold (warm) center to represent temperature minimum (maximum), and a fresh (salty) center to represent salinity minimum (maximum).

6.5.3 Temperature

(a) *Sea surface.* Although monthly SST field (Fig. 6.14) shows an evident seasonal variation, the Subpolar Front exists continuously through the year. Its position is quite stationary, but its intensity strengthens in the winter (especially the east part) and weakens in the summer. Such a pattern is similar to earlier description (Maizuru Marine Observatory 1997). The location of the Subpolar Front in spring is quite consistent with Isoda and Saitoh's (1988) estimations using ten NOAA-8 Advanced Very High Resolution Radiometer (AVHRR) images in spring 1984.

The SST is always found higher than 5°C year-round in the Ulleung/Tsushima Basin and the Yamato Basin, which is consistent with Kim and

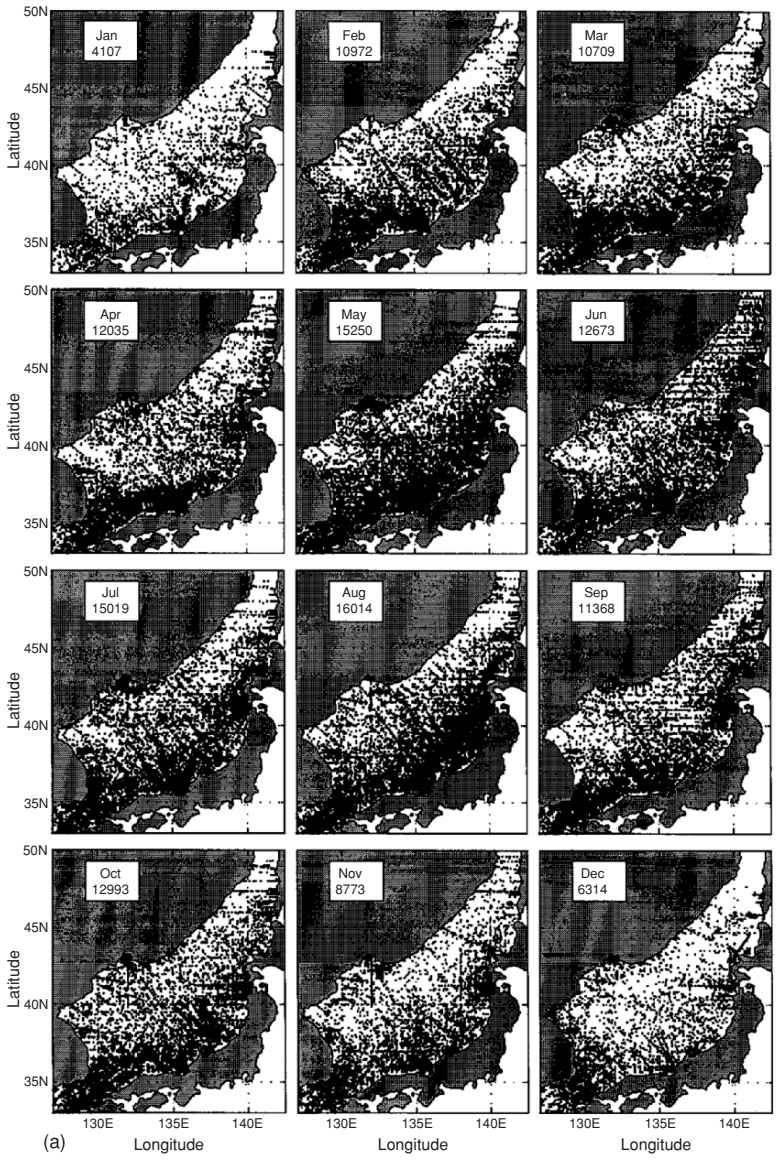

Fig. 6.12. Spatial distribution of the MOODS stations during 1930–1997 (**a**) temperature, and (**b**) salinity (from Chu et al. 2001a, Journal of Physical Oceanography) Yearly temperature (Fig. 6.13a) and salinity (Fig. 6.13b) profile numbers show temporally uneven distribution with almost no observations in the entire Japan Sea in certain years (e.g., 1944, 1989 for temperature, and 1944, 1987–1993 for salinity) and many observations in other years (e.g., nearly 6,500 temperature profiles in 1969, and 3,700 salinity profiles in 1967). Spatial and temporal irregularities along with the lack of data in certain regions must be carefully weighted in order to avoid statistically induced variability.

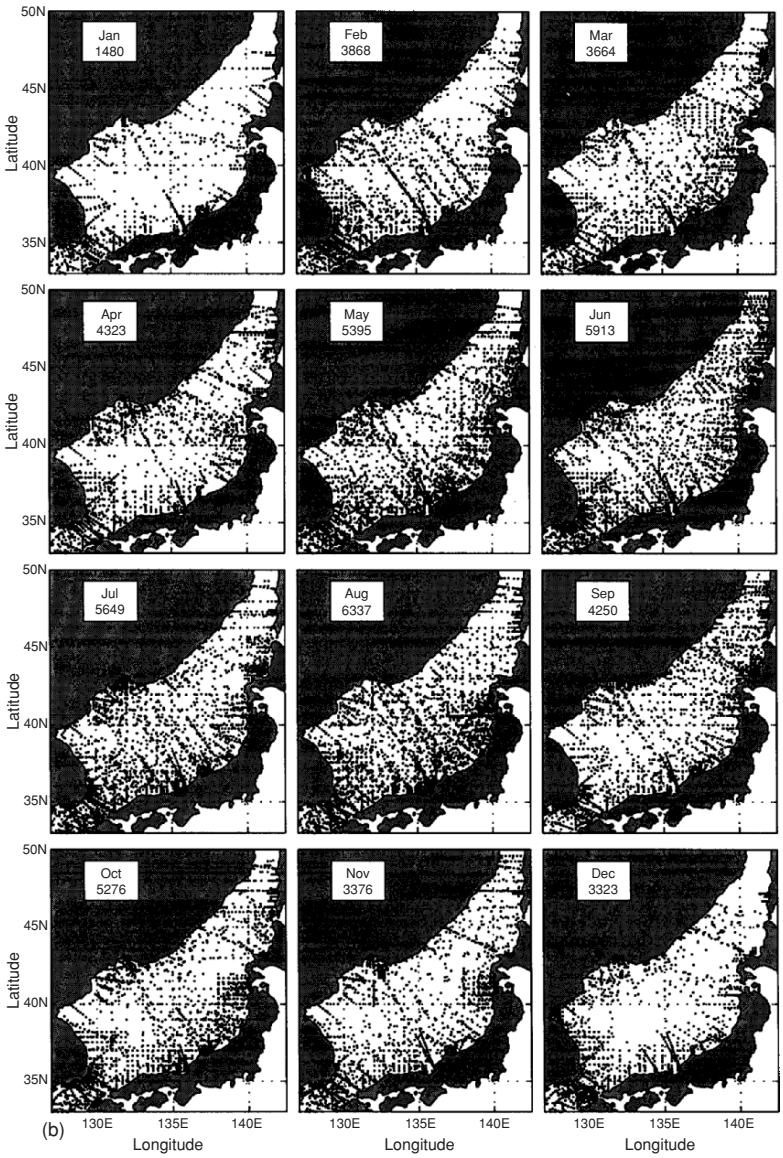

Fig. 6.12. Continued.

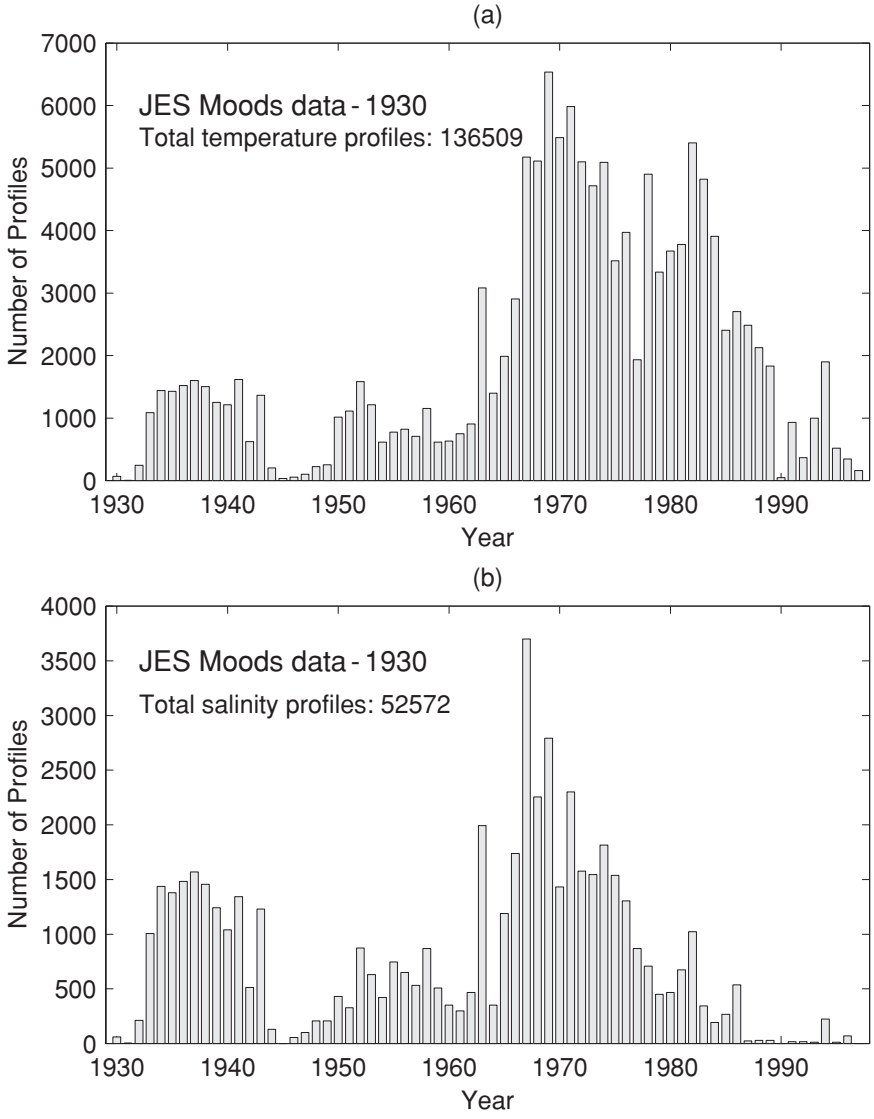

Fig. 6.13. Temporal distribution of the MOODS stations during 1930–1997 (**a**) temperature, and (**b**) salinity (from Chu et al. 2001a, Journal of Physical Oceanography)

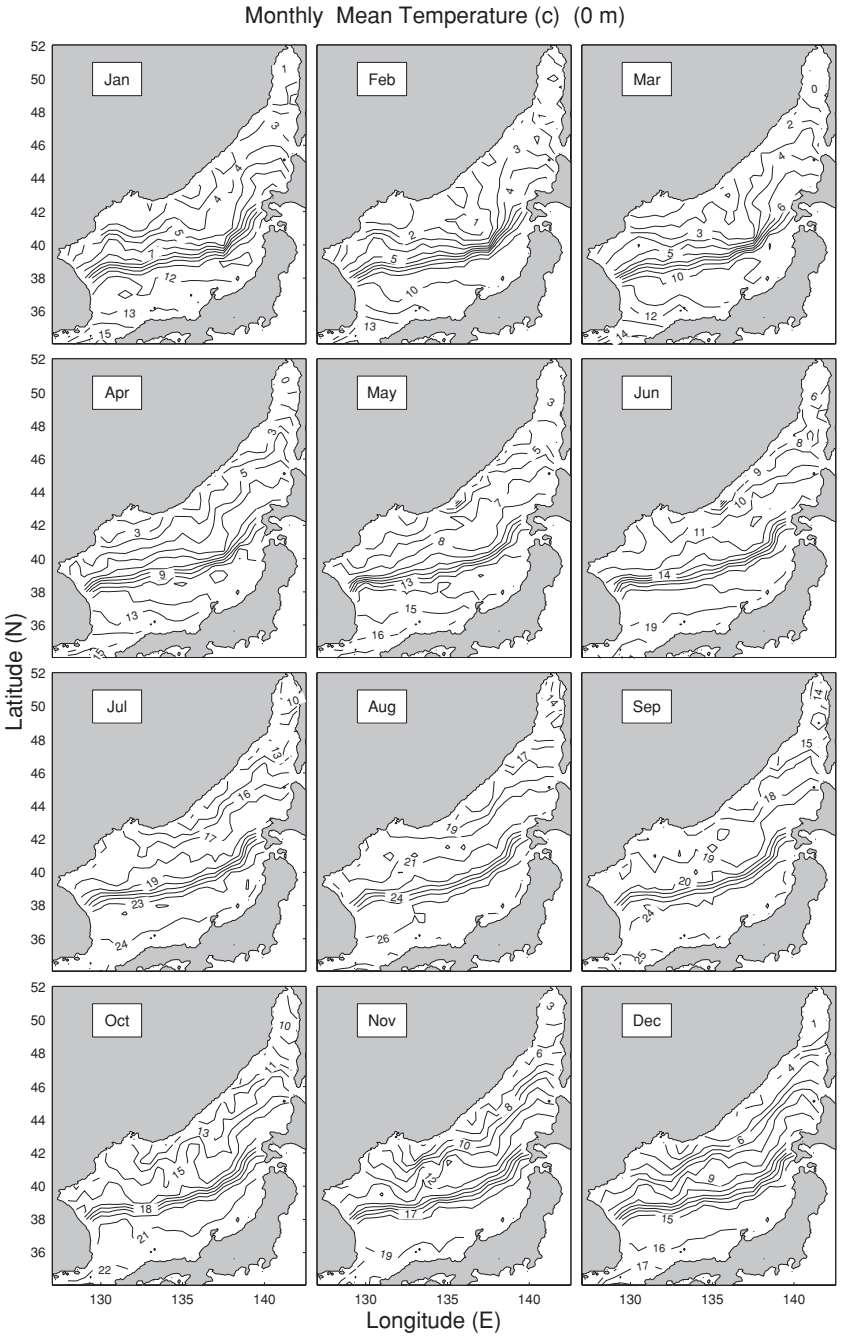

Fig. 6.14. Monthly mean temperature (°C) field at the ocean surface (from Chu et al. 2001a, Journal of Physical Oceanography)

Kim (1999) observational studies. The maximum SST gradient is found as 16°C/100 km near 137°E, 40°N in February and March, and the minimum SST gradient is found as 8°C/100 km from July to September. The SST gradient across the Subpolar Front is two times as strong in the winter as in the summer. The weakening of the Subpolar Front in the summer is caused by the faster warming of the water mass north of this Front than south of the Front in spring. A second front occurs north of the Subpolar Front (bifrontal structure) during the fall-to-winter transition season, especially in November and December. This front parallels the Russian coast with the maximum SST gradient around 4°C/100 km in November.

(b) *Temperature at intermediate level (150-m).* The seasonal thermal variability at the 150 m depth is much weaker than at the surface (Fig. 6.15). The Subpolar Front still occurs throughout the year and is located at almost the same location as at the surface. At the north of the Subpolar Front, temperature is uniformly cold (1°–3°C) throughout the year; south of the Subpolar Front, temperature changes from 5° to 9°C. The Subpolar Front meandering at 131°E, 134°E, and 138°E forms several mesoscale eddies. The meandering near Okin Gunto (134°E) in spring was previously reported by Isoda and Saitoh (1988; 1993). Besides, a second front occurs (bifrontal structure) south of the Subpolar Front along the west coast of Japan during the winter and spring seasons.

(c) *Zonal cross-sections (37°N and 43°N).* The zonal cross-sections (37°N and 43°N) of the monthly mean temperature show a strong seasonal/permanent thermocline structure south of the Subpolar Front (Fig. 6.16a) and a strong seasonal/weak permanent thermocline structure north of the Front (Fig. 6.16b).

South of the Front at 37°N (Fig. 6.16), the permanent thermocline is located at 80–125 m and appears all year round with the maximum strength (0.12°C m^{-1}) in August. Above it, the seasonal thermocline occurs from the surface to 50 m depth in June (0.15°C m^{-1}), which intensifies during the summer monsoon season to a maximum value of around 0.36°C m^{-1} in August, and weakens in September. In October, the seasonal thermocline erodes and the ocean mixed layer starts to occur. In November, the mixed layer is well established with the temperature near 18°C and the depth around 75 m.

During the prevailing winter monsoon season (December–March), the mixed layer deepens to 80–130 m with a westward uplift of the mixed layer depth: 80 m near the Korean coast and 130 m near the Japanese coast. The mixed layer temperature is around 10°C, starts to warm at a rate of 2°C/month from March to May, and its depth shoals. For example, the mixed layer temperature increases from 12°C in April to 14°C in May, and the mixed layer depth decreases from 50 to 70 m in April to less than 50 m in May. This process (warming and shoaling) continues during the summer monsoon season (June–August).

North of the Subpolar Front at 43°N (Fig. 6.17), the permanent thermocline is quite weak and located near the surface to 300 m depth with an evident westward uplift from the Japanese coast (thickness around 300 m) to

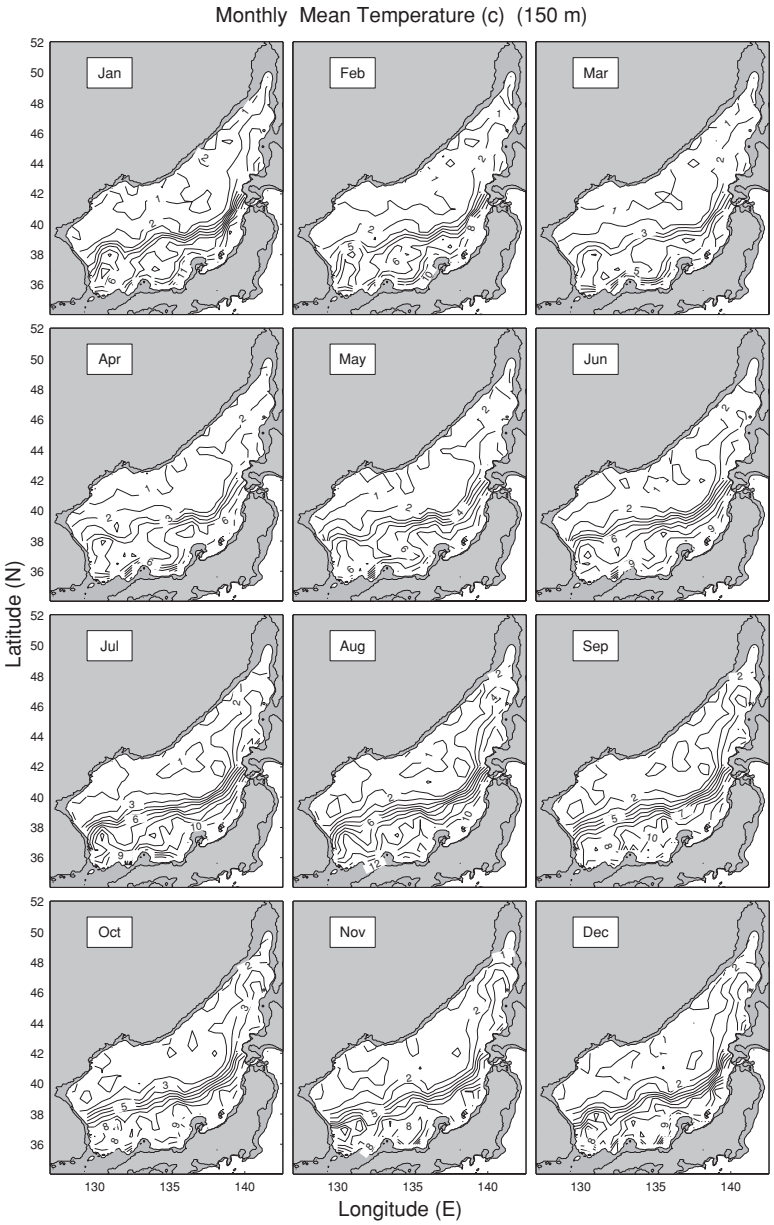

Fig. 6.15. Monthly mean temperature (°C) field at 150 m depth (from Chu et al. 2001a, Journal of Physical Oceanography)

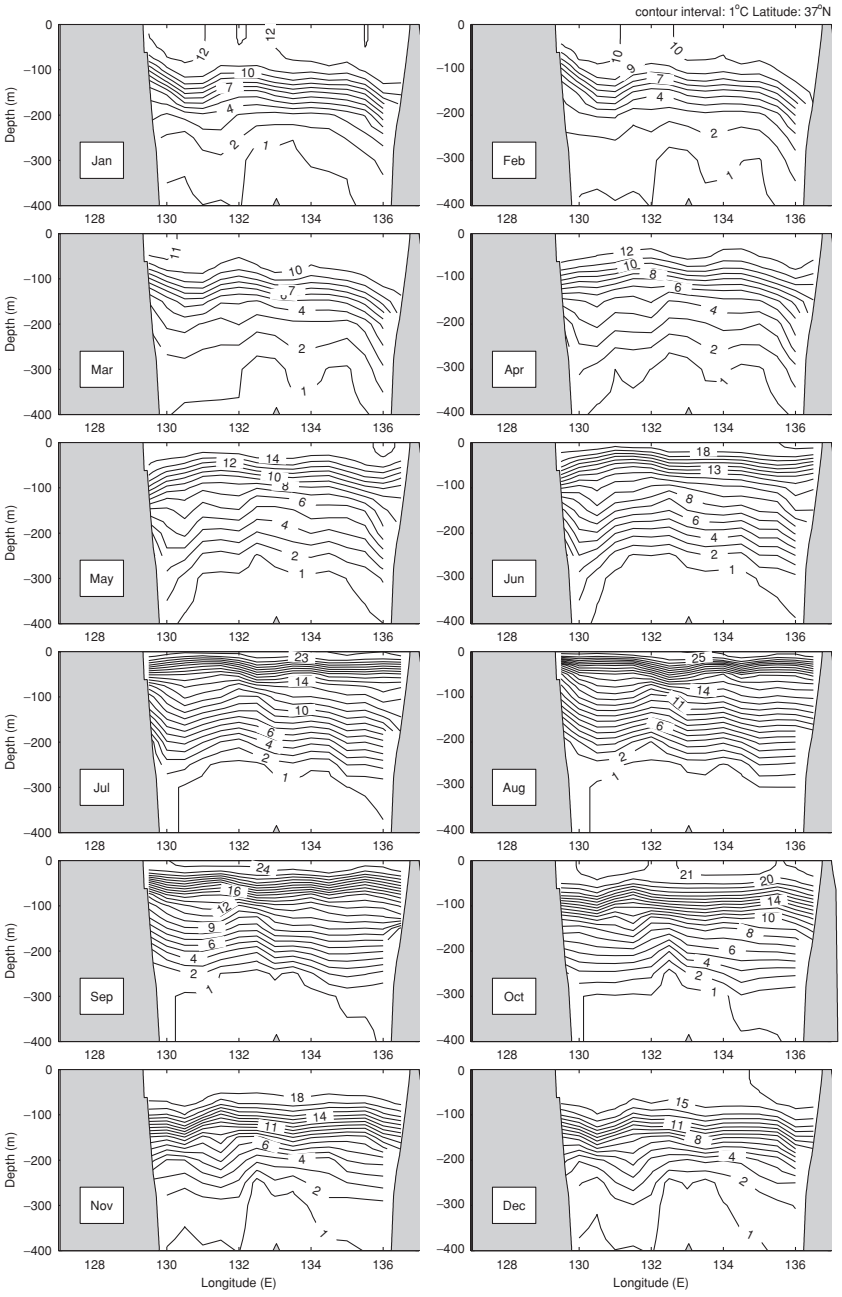

Fig. 6.16. Zonal cross-section of monthly mean temperature (°C) at 37°N. Contour interval: 1°C (from Chu et al. 2001a, Journal of Physical Oceanography)

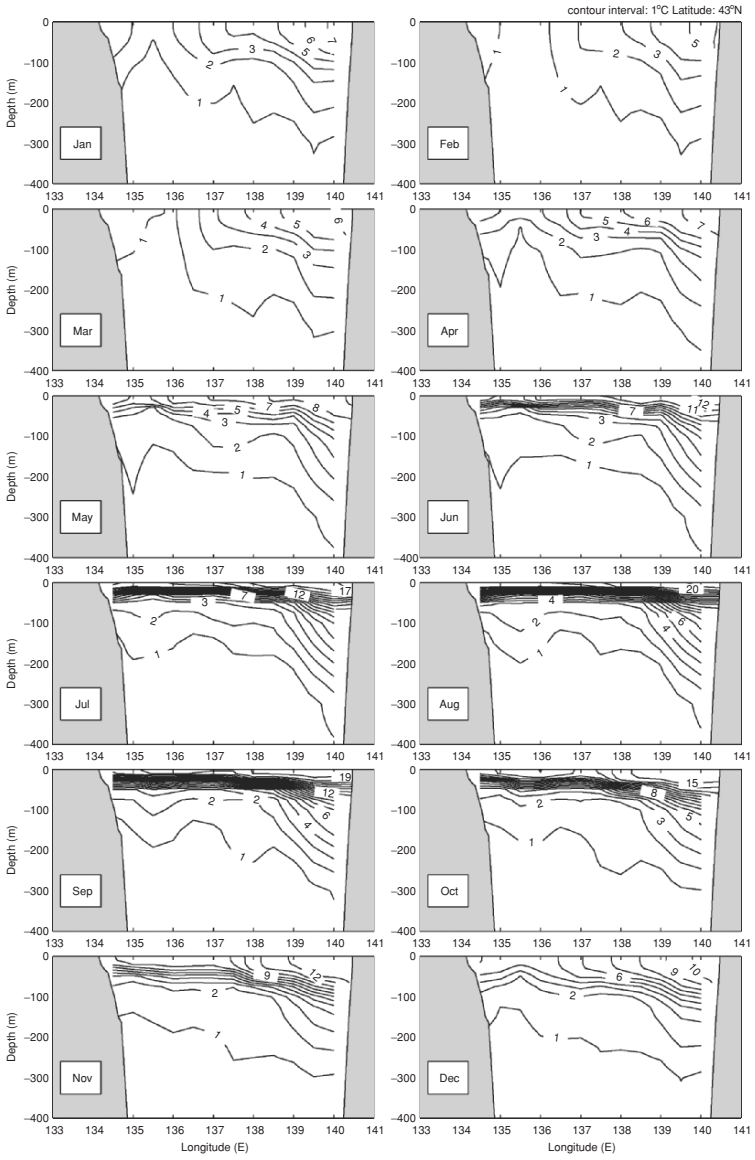

Fig. 6.17. Zonal cross-section of monthly mean temperature (°C) at 43°N. Contour interval: 1°C (from Chu et al. 2001a, Journal of Physical Oceanography)

the Russian coast (thickness around 100 m). The seasonal thermocline occurs from the surface to 50 m depth in May ($0.08°\mathrm{C\,m^{-1}}$), which intensifies during the summer monsoon season to a maximum value of around $0.5°\mathrm{C\,m^{-1}}$ in August and September, and weakens in October. In November, the seasonal

thermocline erodes and becomes the part of the permanent thermocline, which weakens during the prevailing winter monsoon season. In February, the permanent thermocline is so weak that the water column is almost uniformly cold (1°C) west of 136°E and weakly stratified ($\leq 0.01°C\,m^{-1}$) east of 136°E.

(d) *Latitudinal cross-section* (135°E). The strong north–south thermal asymmetry across the Subpolar Front is also identified from the latitudinal cross-section (135°E) of the monthly mean temperature (Fig. 6.18). During the prevailing winter monsoon season (December–March), the permanent thermocline is identified at 100–250 m depths south of the Subpolar Front with a vertical temperature gradient weakening from December (near $0.1°C\,m^{-1}$) to March (near $0.05°C\,m^{-1}$). The permanent thermocline is identified at 25–100 m depths north of the Subpolar Front in December with a vertical gradient near $0.06°C\,m^{-1}$, which is much weaker than that south of the Front. From January to March, there is almost no evident thermocline north of the Front.

During the prevailing summer monsoon season (June–August), a shallow seasonal thermocline occurs in the whole Japan Sea basin with a stronger strength north of than south of the Subpolar Front; and overlays relatively uniform water north of the Front and stratified water (the permanent thermocline) south of the Front. A seasonal thermocline appears near the surface at the North of the Front (above 50 m depth) with a vertical gradient enhancing from $0.25°C\,m^{-1}$ in June to $0.36°C\,m^{-1}$ in August.

This strong and shallow thermocline isolates the exchange of the seawater below the thermocline from the atmospheric forcing and makes this water (north of the Subpolar Front under the thermocline) quite uniform. South of the Subpolar Front, a seasonal thermocline is wider (25–100 m depths) and weaker with a vertical gradient around $0.13°C\,m^{-1}$. Such a north–south asymmetric pattern in July was previously presented by Kim and Kim (1999) using the Circulation Research of the East Asian Marginal Seas data taken mainly in the summer of 1995. However, the seasonal thermocline north of the Subpolar Front is stronger from the GDEM data than from the Circulation Research of the East Asian Marginal Seas data.

The seasonal thermocline has a strong asymmetry across the Subpolar Front. North of the Subpolar Front, the seasonal thermocline occurs near the surface in April and May, enhances drastically during the summer monsoon season, survives in Fall, and is still quite strong with a vertical gradient of $0.12°C\,m^{-1}$ in November. It weakens drastically in December. South of the Subpolar Front, the seasonal thermocline occurs in the summer monsoon season, survives in the early fall, and disappears in November.

6.5.4 Salinity

(a) *Sea surface.* The monthly sea surface salinity field (Fig. 6.19) shows a strong seasonal variation with less (more) horizontal variability in the winter (summer). The saline Kuroshio water (>34.2 ppt) enters the Japan Sea

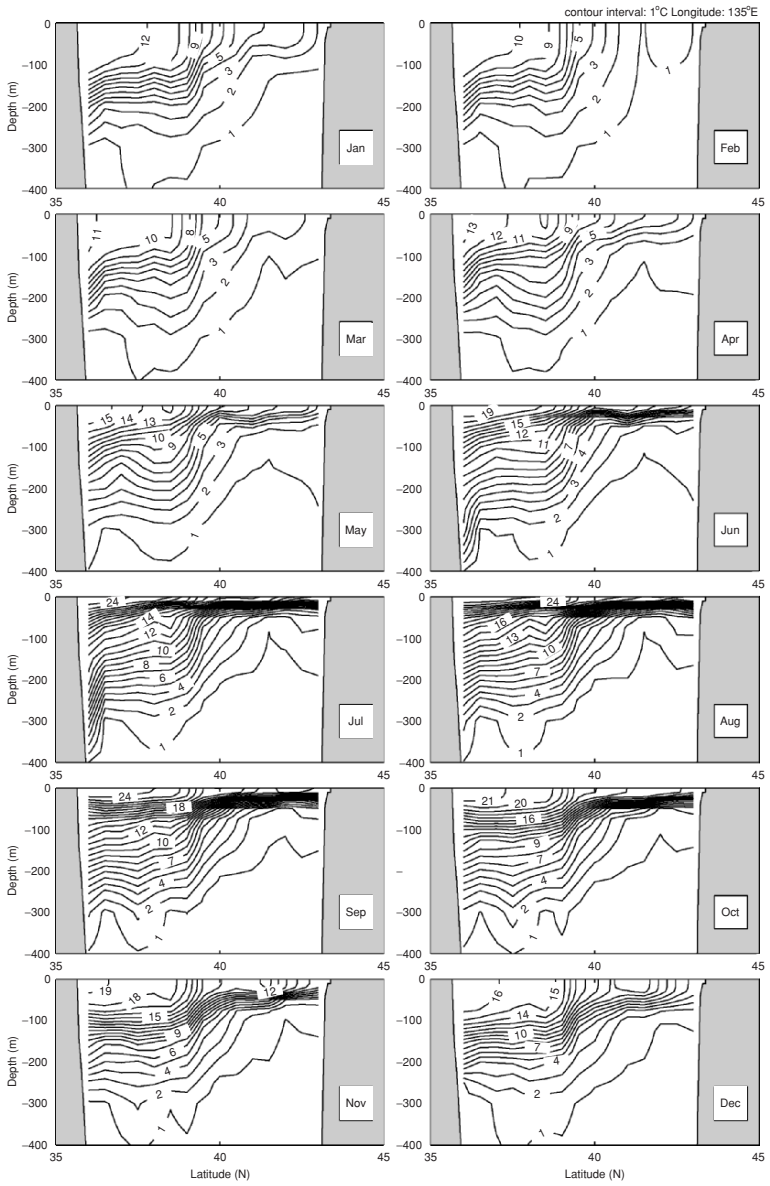

Fig. 6.18. Latitudinal cross-section of monthly mean temperature (°C) at 135°E. Contour interval: 1°C (from Chu et al. 2001a, Journal of Physical Oceanography)

from the Tsushima/Korean Strait into the Japan Sea and forms two permanent salty centers located in the northern Japan Basin (west of the Hokkaido Island) with the salinity higher than 34.0 ppt, and the area between the Ulleung/Tsushima and Yamato Basins with the maximum salinity of 34.3 ppt in

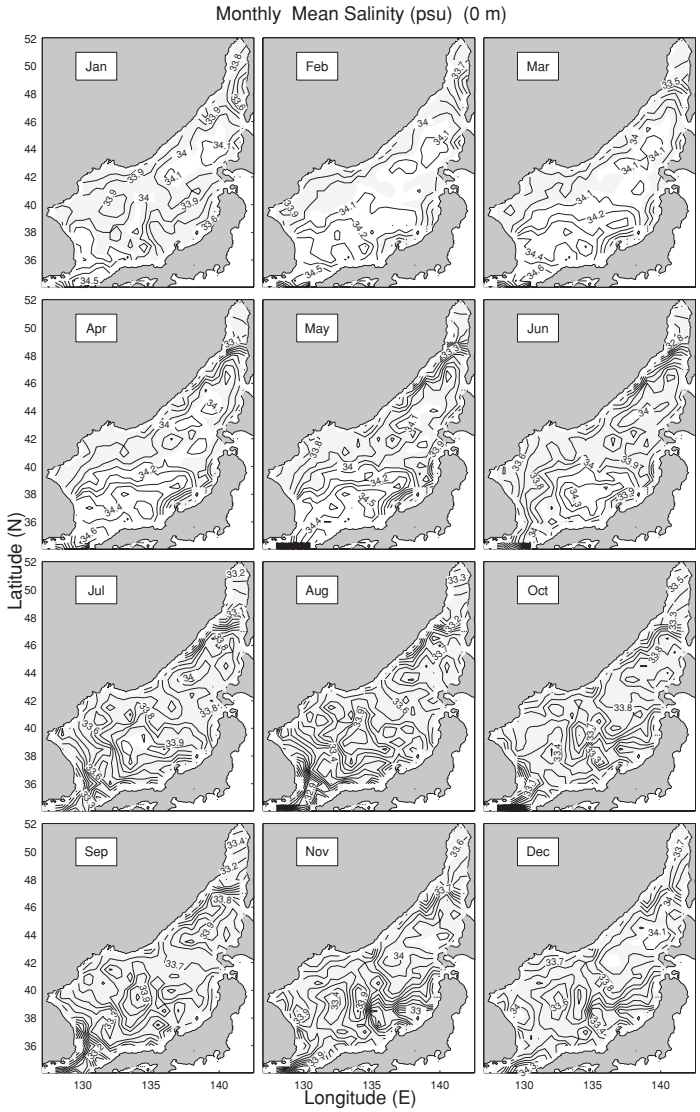

Fig. 6.19. Monthly mean salinity (ppt) field at the ocean surface (from Chu et al. 2001a, Journal of Physical Oceanography)

June, respectively. The salty center has less seasonal variation in the northern Japan Basin than the Ulleung/Tsushima and Yamato Basins. The winter (February) field is consistent with that reported by Kim and Kim (1999) using the data set of the Japan Oceanographic Data Center during 1930 to 1990.

(b) *Intermediate level (150 m).* Figure 6.20 shows horizontal depictions of the monthly mean salinity at 150 m depth with a contour interval of 0.1 ppt.

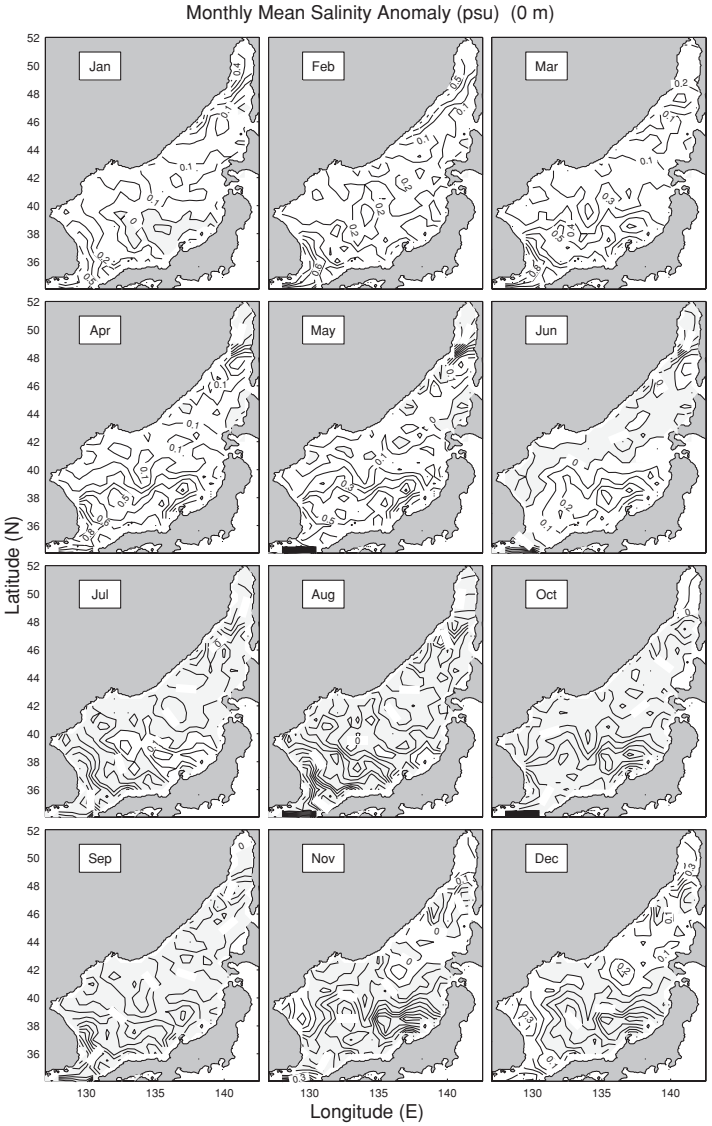

Fig. 6.20. Monthly mean salinity (ppt) field at 150 m depth (from Chu et al. 2001a, Journal of Physical Oceanography)

The depth of 150 m corresponds to the middle level of the Japan Sea Intermediate Water (low salinity) as well as the High Salinity Intermediate Water (high salinity).

Low salinity in the Japan Sea Intermediate Water (less than 34.06 ppt, shaded areas in Fig. 6.20) dominates the western Japan Basin and the Ulle-

ung/Tsushima Basin. It expands eastward during the summer monsoon season (June–September) and retreats westward during the winter monsoon season (December–March).

High salinity of the High Salinity Intermediate Water occupies the eastern Japan Basin. This is consistent with earlier work by Kim and Kim (1999). The saline water occupies the east and south and less of it appears in the north and west, especially in the northwestern boundary. The isohaline of 34.1 is colocated with the Subpolar Front (Fig. 6.15) with the salinity above (below) 34.1 in the south (north) of the Front. Salinity is relatively uniform (34.0–34.1 ppt) throughout the year, north of the Subpolar Front. South of the Subpolar Front the salinity changes from 34.1 to 34.5 ppt.

(c) *Zonal cross-sections* ($37°N$ and $43°N$). The zonal cross-sections (37°N and 43°N) of the monthly mean salinity show an evident salinity minimum south of the Subpolar Front (Fig. 6.21) and absence of a salinity minimum north of the Front (Fig. 6.22). This consistency exists with many earlier studies such as Miyazaki (1952,1953), Miyasaki and Abe (1960), Kim and Chung (1984), Senjyu (1999), and Kim and Kim (1999).

South of the Subpolar Front at 37°N (Fig. 6.21), a strong (seasonal) halocline occurs from the surface to 30 m depth in June ($0.01\,\mathrm{ppt\,m^{-1}}$), which intensifies during the summer monsoon season to a maximum value of around $0.03\,\mathrm{ppt\,m^{-1}}$ in August, and weakens from September to December.

In January, the halocline erodes and disappears. During the summer monsoon season (June–September), the salinity minimum shifts eastward from the Ulleung/Tsushima Basin (131°–133°E) in June to the southern Yamato Basin (132°–135°E) in July–September. A horizontally oriented SMAX ($S > 34.2$ ppt) appears above the salinity minimum with the interface at 200–300 m depths.

In October, this horizontally oriented salinity maximum is broken into two parts with each part enclosed by the 34.2 ppt isoline. A narrow relatively low salinity area, sandwiched by the two SMAX centers, occurs in the central Ulleung/Tsushima Basin (near 132°E) beneath 100 m depth and strengthens from November to January accompanying the erosion of the surface halocline.

In January, the near surface halocline disappears, the salinity minimum (enclosed by 34.1 ppt isoline) appears in the Ulleung/Tsushima Basin (131°–133°E) and reaches the surface, eventually the two salinity maximum centers weaken (especially the west one). The salinity minimum expands horizontally, descending vertically, and becomes very evident in February. From February to June, the salinity minimum continues to descend. The top of the salinity minimum occurs at 150–200 m depths in February and at 200–300 m in April–June.

North of the Subpolar Front at 43°N (Fig. 6.22), the salinity minimum shows up in the upper layer (above 100 m) of the western Japan Basin (west of 136°E) all the year round. This is consistent with Kim and Kim's (1999) identification that the Japan Sea Immediate Water in the western Japan Basin is characterized by a low salinity ($S < 34.06$). The high salinity water ($S >$

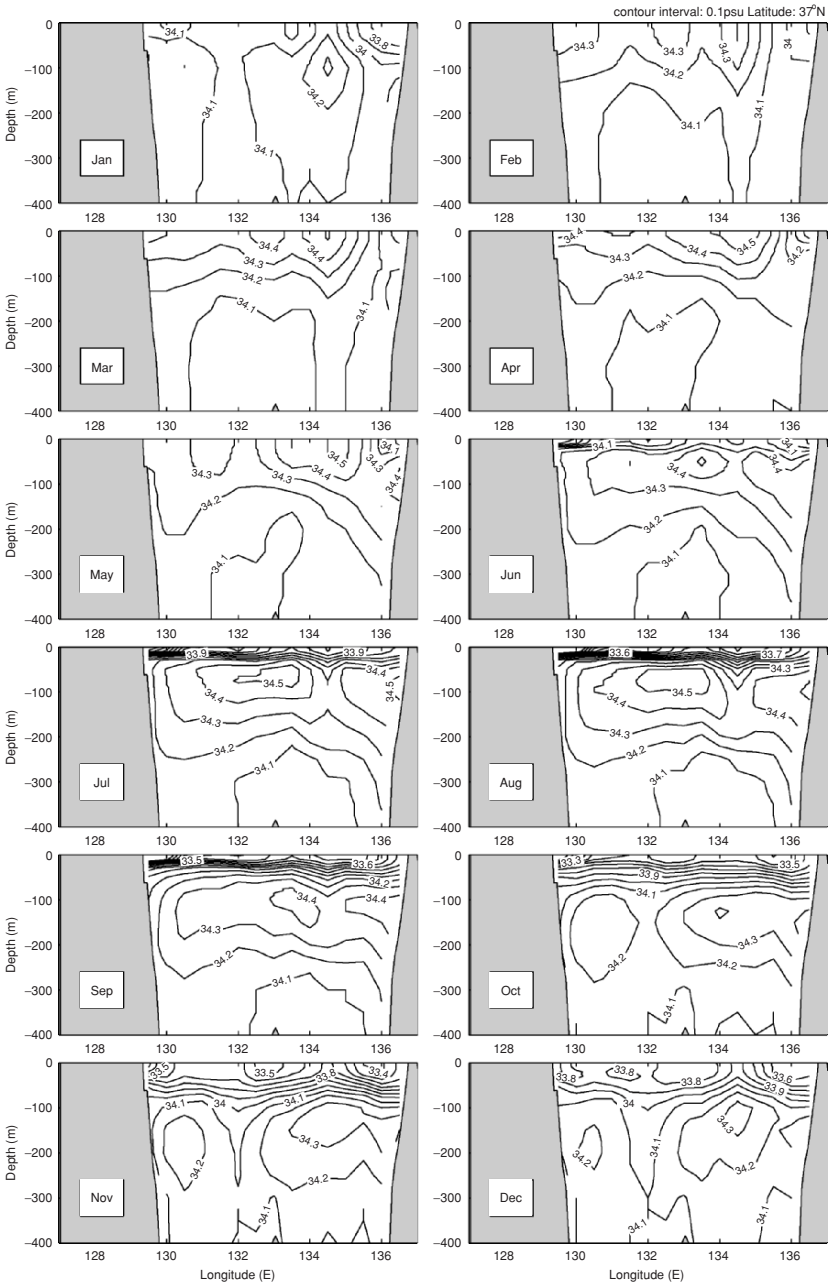

Fig. 6.21. Zonal cross-section of monthly mean salinity (ppt) at 37°N. Contour interval: 0.1 ppt (from Chu et al. 2001a, Journal of Physical Oceanography)

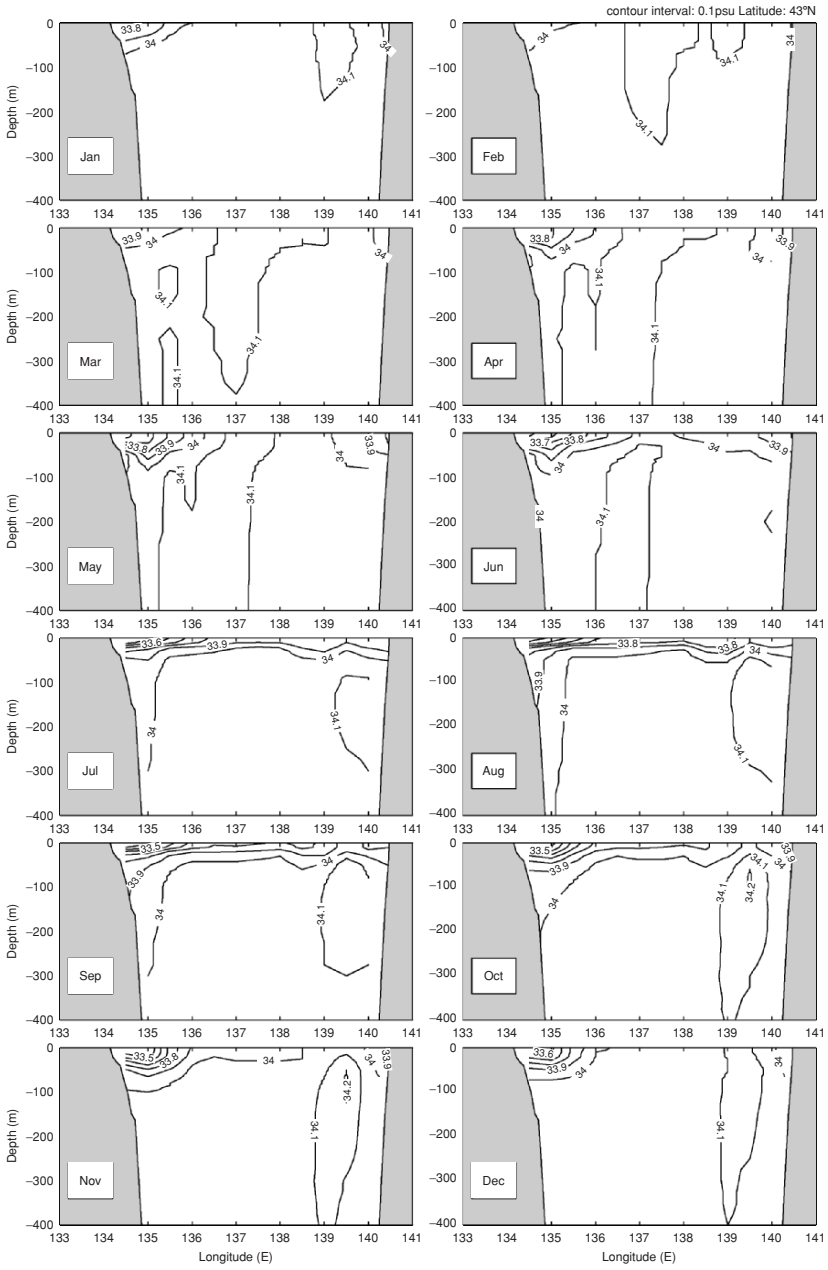

Fig. 6.22. Zonal cross-section of monthly mean salinity (ppt) at 43°N. Contour interval: 0.1 ppt (from Chu et al. 2001a, Journal of Physical Oceanography)

34.1 ppt) of the High Salinity Immediate Water appears in the central (136°–138°E) and the eastern (138.5°–140°E) Japan Basin. The eastern Japan Basin salinity maximum appears almost all the year round except the spring season (March–May). The central Japan Basin salinity maximum is not as evident as the eastern one except in February and March.

(d) *Latitudinal cross-section* (135°E). The strong north–south haline asymmetry across the Subpolar Front is also identified from the latitudinal cross-section (135°E) of the monthly mean salinity: the appearance (disappearance) of the salinity minimum south (north) of the Subpolar Front (Fig. 6.23). South of the Subpolar Front, the salinity minimum ($S < 34.06$ ppt) occurs during the summer monsoon season (July–October) underneath a horizontally oriented salinity maximum with a salty core ($S > 34.5$ ppt) at 100 m depth. The salinity maximum with a salty core ($S = 34.3$ ppt) was observed in October 1969 when a hydrographic survey for the whole Japan Sea basin was carried out by the Japan Meteorological Agency (Kim and Kim 1999). The interface between the salinity minimum and maximum is located at 200–300 m depth. During the winter monsoon season, the salinity minimum is not evident. North of the Subpolar Front, high salinity water ($S > 34.1$ ppt) of the High Salinity Intermediate Water appears in the central Japan Basin (40°–43°N) with strengthening in the winter and weakening in the summer.

6.5.5 Absolute Velocity

The inverted absolute velocity field (Fig. 6.24) coincides with earlier descriptions of the Japan Sea circulation (e.g., Uda 1934; Suda and Hidaka 1932; Suda et al. 1932). However, the currents at the four major straits are not well inverted. For example, the velocity at the Tsushima/Korea Strait is too small, and there is no velocity inverted at the other straits such as the Tartar Strait. This may be caused by the narrowness and shallowness of the straits.

The inverted absolute velocity field shows an evident branching of the Tsushima Warm Current. North of 35°N, the Tsushima Warm Current bifurcates into an eastern channel (first branch) and a western channel. The strength of the Tsushima Warm Current at both channels reduces with depth. The flow through the western channel (i.e., the East Korean Warm Current) closely follows the Korean Coast until it separates near 37°–38°N into two branches: the off-shore branch (or the second branch) follows the Polar Front to the western coast of Hokkaido Island, and the long-shore branch (or the third branch), moves northward (i.e., the East Korean Warm Current). Such a three-branch pattern was first identified by Suda and Hidaka (1932) and Suda et al. (1932) using hydrographic and current meter data observed from the month of June to September in 1929 and in 1930, respectively. Since then, the existence of three branches has been believed to be the typical Tsushima Warm Current flow pattern. Using temperature and salinity data mainly obtained in 1973, Kawabe (1982a) investigated the seasonal variation of the Tsushima Warm Current branching and found that the first branch exists in

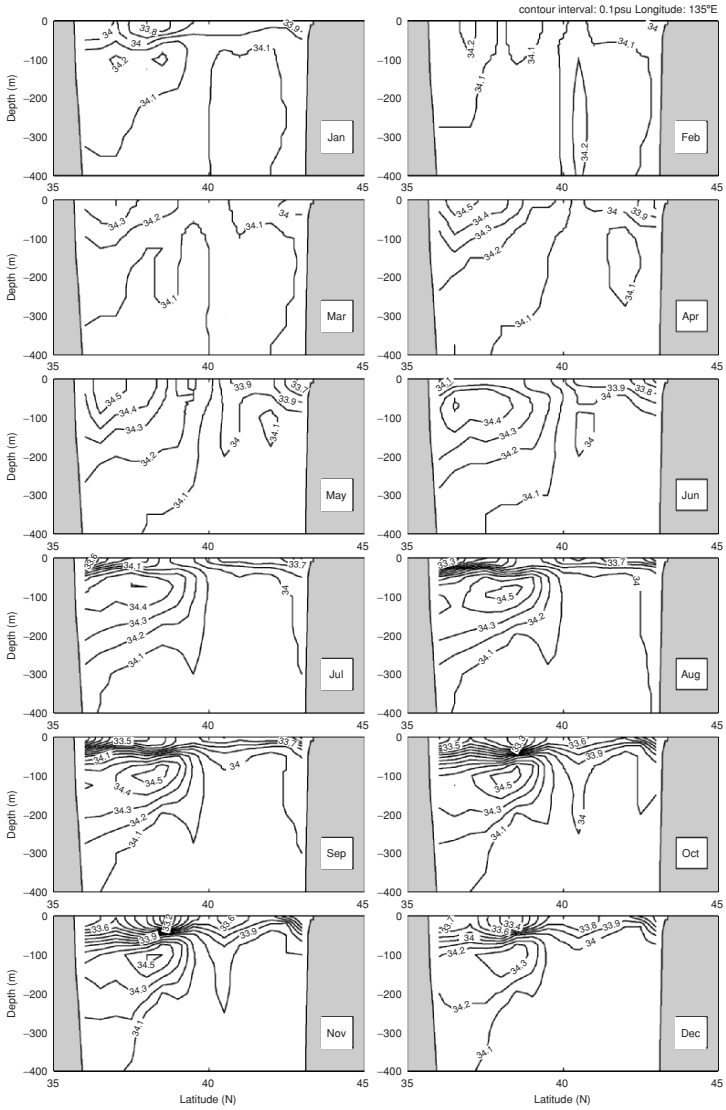

Fig. 6.23. Latitudinal cross-section of monthly mean salinity (ppt) at 135°E. Contour interval: 0.1 ppt (from Chu et al. 2001a, Journal of Physical Oceanography)

spring and summer, the second branch only in summer from the month of June to August, and the third branch in all seasons. His observational results were simulated using a two-layer numerical model (Kawabe 1982b; Sekine 1986).

The inverted flow through the eastern channel (first branch) closely follows the Japanese coast (i.e., Japan Near-Shore Branch) and is weaker than the flow through the western channel (Fig. 6.24). The maximum speed of the first

branch is found to be around $0.1\,\mathrm{m\,s^{-1}}$, occurring near the Japanese coast (135°E, 35.5°N) at the surface. The Japan Near-Shore Branch is too weak to be identified in winter (December–February). In March, the Japan Near-Shore Branch starts to occur along the Japanese coast, and strengthens in spring and reaches the maximum velocity in July. This coincides with Kawabe's (1982a) observational results.

The inverted flow along the Subpolar Front (second branch) may be called as the Polar Front Current. The maximum speed of the Polar Front Current is found at the surface around $0.2\,\mathrm{m\,s^{-1}}$ (Fig. 6.24). An asymmetric cyclonic gyre is found in the MidJapan Sea (135°–140°E, 38°–44°N) in the winter monsoon season (December–March) with the flow associated with the Polar Front Current as the southern and eastern flanks and the flow from the north (MidJapan Sea cold current) as the northern and western flanks. The Polar Front Current has a weak seasonal variation in flow pattern and a strong seasonal variation in current speed. The seasonal variability of this gyre is largely determined by the seasonal variability of the Polar Front Current.

An interesting feature is the out-of-phase variation between the Polar Front Current and the Japan Near-Shore Branch (along the west coast of Japan). For example, the Polar Front Current (Japan Near-Shore Branch) strengthens (weakens) from July to September, and weakens (strengthens) in spring from March to April.

The seasonal variation of the Japan Sea major currents is also shown in the latitudinal cross-section of the monthly mean u-component (Fig. 6.25). Two eastward flowing currents, the Japan Near-Shore Branch (near 36°N) and the Polar Front Current (38°–40°N), are well represented. The Polar Front Current has the maximum speed of $0.22\,\mathrm{m\,s^{-1}}$ (minimum speed of $0.12\,\mathrm{m\,s^{-1}}$) occurring in September (February–April) at the surface. During the summer monsoon season (July–September), the Polar Front Current strengthens (maximum speed increases from $0.18\,\mathrm{m\,s^{-1}}$ to $0.22\,\mathrm{m\ s^{-1}}$) and the Japan Near-Shore Branch weakens (maximum speed decreases from $0.12\,\mathrm{m\,s^{-1}}$ to $0.04\,\mathrm{m\,s^{-1}}$). During winter monsoon season (December–April), the Polar Front Current weakens (maximum speed decreases from 0.18 to $0.12\,\mathrm{m\,s^{-1}}$) and the Tsushima Warm Current strengthens (maximum speed increases from $0.02\,\mathrm{m\,s^{-1}}$ in January to $0.1\,\mathrm{m\,s^{-1}}$ in April). The volume transport of the Polar Front Current shows an evident seasonal variation with the maximum value of 1.32 Sv ($1\,\mathrm{Sv} = 10^6\,\mathrm{m^3\,s^{-1}}$) in November–December and the minimum value of 0.88 Sv in April (Fig. 6.26).

This example shows the usefulness of the P-vector method. The inverted absolute geostrophic velocities represent the Japan Sea circulation reasonably well, especially the Tsushima Current and its bifurcation. The Polar Front Current has a weak seasonal variation in flow pattern, a strong seasonal variation in current speed, and out-of-phase variability with the Tsushima Warm Current. When the Polar Front Current strengthens from July ($0.18\,\mathrm{m\,s^{-1}}$) to September ($0.22\,\mathrm{m\,s^{-1}}$), the Tsushima Warm Current weakens from 0.12 to $0.04\,\mathrm{m\,s^{-1}}$. When the Polar Front Current weakens from

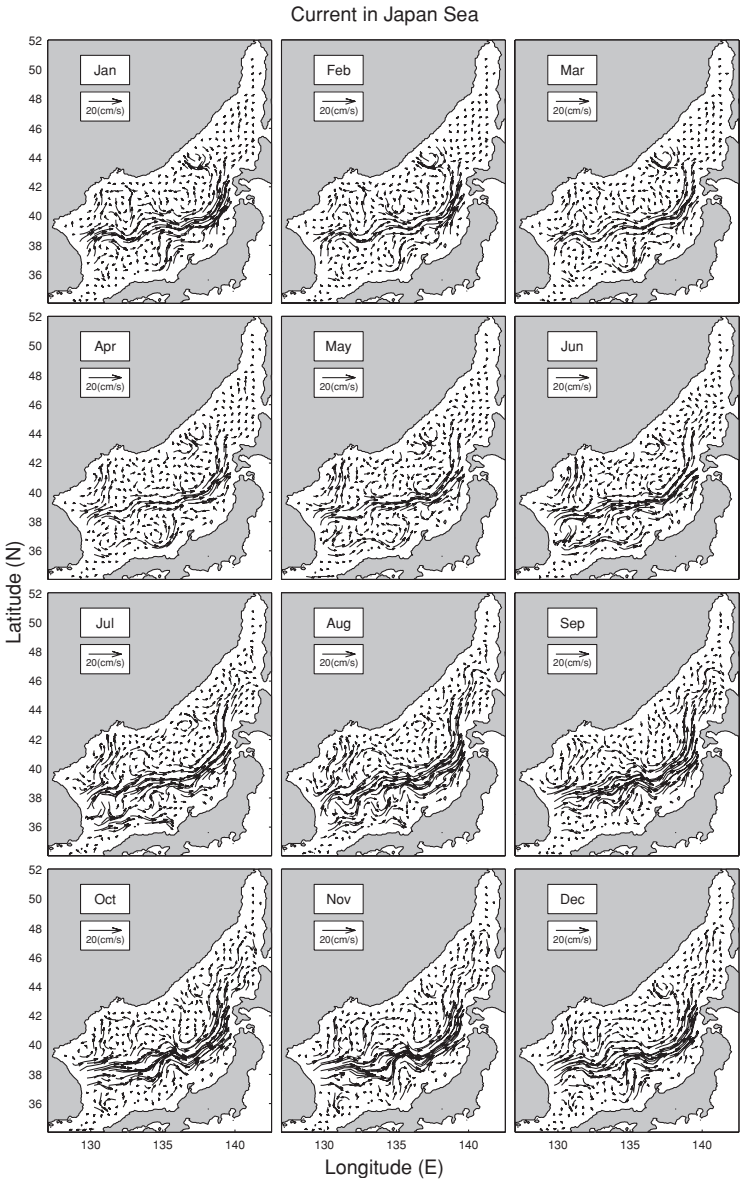

Fig. 6.24. Inverted monthly mean surface circulation (from Chu et al. 2001a, Journal of Physical Oceanography)

January ($0.18\,\mathrm{m\,s^{-1}}$) to April ($0.12\,\mathrm{m\,s^{-1}}$), the Tsushima Current strengthens from 0.02 to $0.1\,\mathrm{m\,s^{-1}}$. The seasonal variability of the MidJapan Sea cyclonic gyre is largely determined by the seasonal variability of the Polar Front Current. The volume transport of the Polar Front Current has the maximum

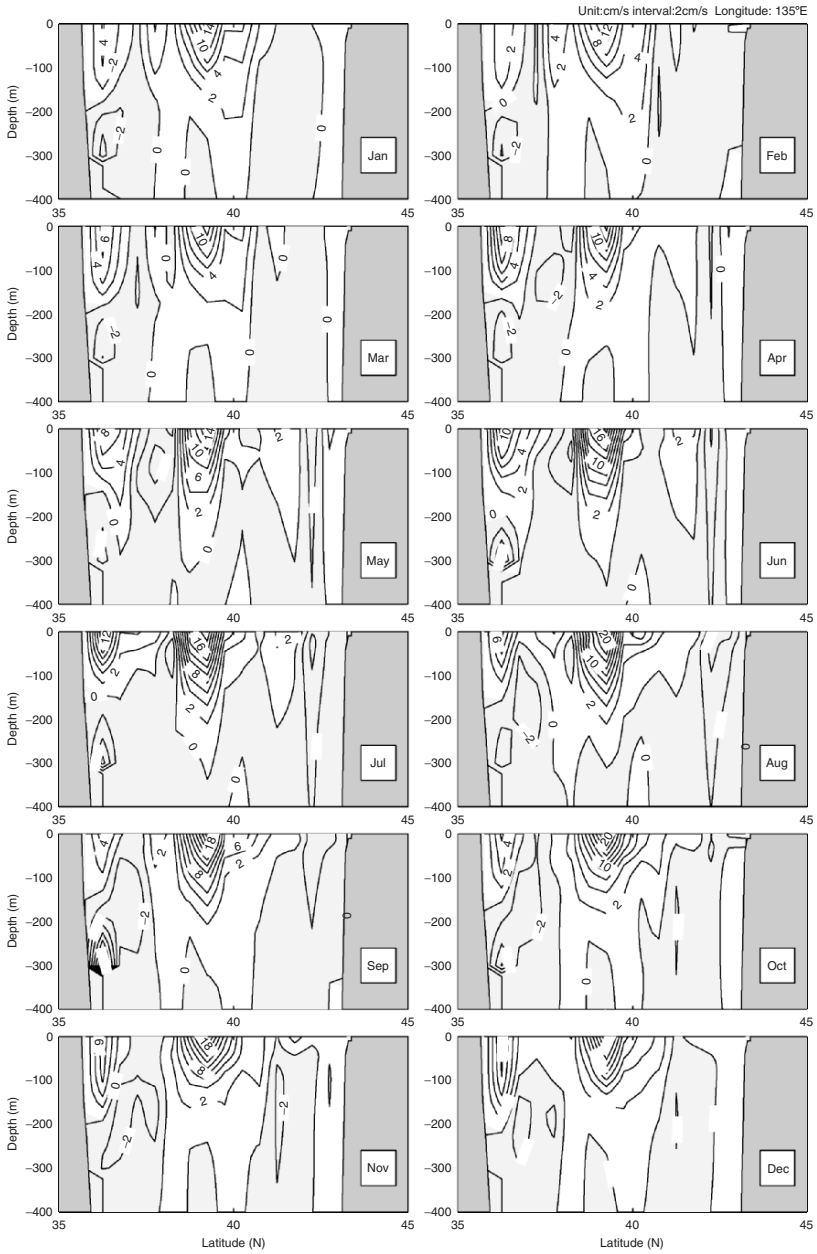

Fig. 6.25. Latitudinal cross-section of monthly mean u velocity ($10^{-2}\,\mathrm{m\,s^{-1}}$) at 135°E. Contour interval: $10^{-2}\,\mathrm{m\,s^{-1}}$ (from Chu et al. 2001a, Journal of Physical Oceanography)

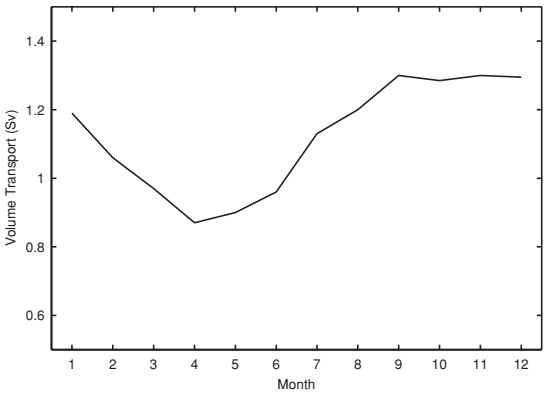

Fig. 6.26. Monthly variation of the volume transport (Sv) of the Polar Front Current at 135°E cross-section (from Chu et al. 2001a, Journal of Physical Oceanography)

value of 1.32 Sv in November–December and the minimum value of 0.88 Sv in April.

6.6 Isopycnal Coordinate System

In this section, the South China Sea is used as an example to illustrate the P-vector inverse method in the isopycnal-coordinate system (Chu and Li 2000; Chu et al. 2002a).

6.6.1 South China Sea

South China Sea, the largest marginal sea in the West Pacific Ocean, is separated from adjacent oceans by a chain of islands. It contains a broad shallow shelf on the south, extending along the Vietnamese-Chinese coast to the Taiwan Strait on the north, a deep sea basin in the center, and a dangerous ground near Nansha with numerous reef islands over the southeast (Fig. 6.27). It has a bottom topography that makes it a unique semienclosed ocean basin overlaid by a pronounced monsoon surface wind. Extensive continental shelves (less than 100 m deep) are found on the western and southern parts, while steep slopes with almost no shelves are found in the eastern part of South China Sea. The deepest water is confined to a bowel-type trench and the maximum depth is approximately 4,700 m. The South China Sea joins the Pacific Ocean through the Luzon Strait between Taiwan and Philippine. The combination of geometry, connectivity with the Pacific Ocean, and strongly variable atmospheric forcing contributes to the complex dynamics of the flow in that region (Metzger 1996).

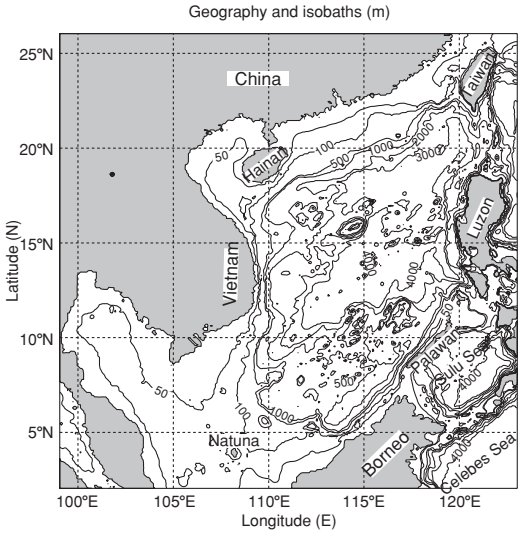

Fig. 6.27. Geography and isobaths showing the bottom topography of the South China Sea (from Chu and Li 2000, Journal of Physical Oceanography)

6.6.2 Oceanic Conditions

The Kuroshio, originating from the North Equatorial Current, flows northward as a western boundary current east of Luzon and Taiwan (Nitani 1970). The Luzon Strait is the principal passage through which the Pacific water enters the South China Sea; therefore the mass transport through the Luzon Strait is critical in determining the characteristics of the South China Sea waters (Shaw 1989, 1991). For example, Hu et al. (1992) believed this flow to contribute to currents in Taiwan Strait. However, Li et al. (1992) showed, by using a numerical model, that this flow did not contribute to currents in the Taiwan Strait. The volume transport through the Luzon Strait is uncertain. Different authors reported values ranging from 8 to 10 Sv by Huang et al. (1994) to 3 Sv outflow in summer and 3 Sv inflow in winter by Wyrtki, (1961a, b). Metzger (1996) estimated that the mean Kuroshio intrusion through the Luzon Strait is around 2.4–4.4 Sv (higher resolution with lower transport values) using the Navy's Layered Ocean Model forced by wind stress climatology having various resolutions.

The seasonally reversing monsoon winds also play an important role in determining the upper ocean circulation (Shaw and Chao 1994). From April to August, the weaker southwesterly summer monsoon winds result in a wind stress of over $0.1\,\mathrm{N\,m^{-2}}$ and drive a northward coastal jet off Vietnam coast and an anticyclonic basin-scale circulation. From November to March, the stronger northeasterly winter monsoon winds correspond to a maximum wind stress of nearly $0.3\,\mathrm{N\,m^{-2}}$ and cause a southward coastal jet and cyclonic basin-scale circulation. Such a seasonal variability of the surface circulation

was simulated by several numerical models (e.g., Chu et al. 1998c, 1999b–d, 2000b; Chao et al. 1996). However, Metzger (1996) pointed out that the surface currents observed by Wyrtki, (1961a, b) are subjected to Ekman drift in this highly variable wind regime.

Seasonal occurrence of the South China Sea eddies have been reported by several authors. Dale (1956) and Uda and Nakao (1972) reported a cold eddy off the central Vietnam coast in summer. Nitani (1970) found a cold eddy located northwest of Luzon in summer. Reports from the South China Sea Institute of Oceanology (1985) indicate that a warm-core eddy appears in summer and winter in the central South China Sea, but in summer, it is closer to Vietnam at the surface. Recently, a cold-core eddy was detected in the central South China Sea during December 29, 1993, to January 5, 1994, from the analysis of TOPEX/Poseidon data (Soong et al. 1995). Chu et al. (1997d) and Chu and Chang (1997) identified the existence of a central South China Sea surface warm-core eddy in midMay from a historical data set: the MOODS data. From the composite analysis on the US NCEP monthly SST fields (1982–1994), Chu et al. (1997d) found that during the spring-to-summer monsoon transition (March–May) a warm anomaly (greater than 1.8°C) is formed in the central South China Sea at 112°–119°30'E, 15°–19°30'N. Emery and Csanady (1973) reported that many large stratified lakes and semienclosed marginal seas and estuaries exhibit a persistent cyclonic circulation. Integrating the Navy's Layered Ocean Model to the statistically equilibrium state, Metzger (1996) simulated a persistent cyclonic circulation in the upper layer of the South China Sea with an approximate thickness of 250 m.

Questions arise: is the viewpoint of Emery and Csanady's (1973) or Metzger and Hurlburt's (1996) cyclonic circulation pattern representative for the South China Sea circulations below the mixed layer? What is the seasonal variability of the Kuroshio intrusion through the Luzon Strait? The P-vector method is used to invert the absolute geostrophic circulations (both barotropic and baroclinic parts) on the isopycnal surfaces from the Navy's public domain GDEM climatological monthly mean temperature and salinity data set with 0.5° resolution (Teague et al. 1990).

6.6.3 Monthly Mean Temperature Field

The monthly mean 3-D temperature field obtained from the GDEM dataset is similar to the climatological monthly mean fields directly computed from the MOODS as depicted in Chu et al. (2002c). The SST variation obtained from the GDEM data is quite consistent with earlier investigations based on the NCEP data (Chu et al. 1997d) and based on the MOODS data (Chu et al. 1997c, 2002c).

Figure 6.28 is the horizontal depiction of monthly mean temperature at 150 m depth. The contour interval is 0.5°C. In them, we see that the basin is dominated by a cool pool with several cold centers located northwest of

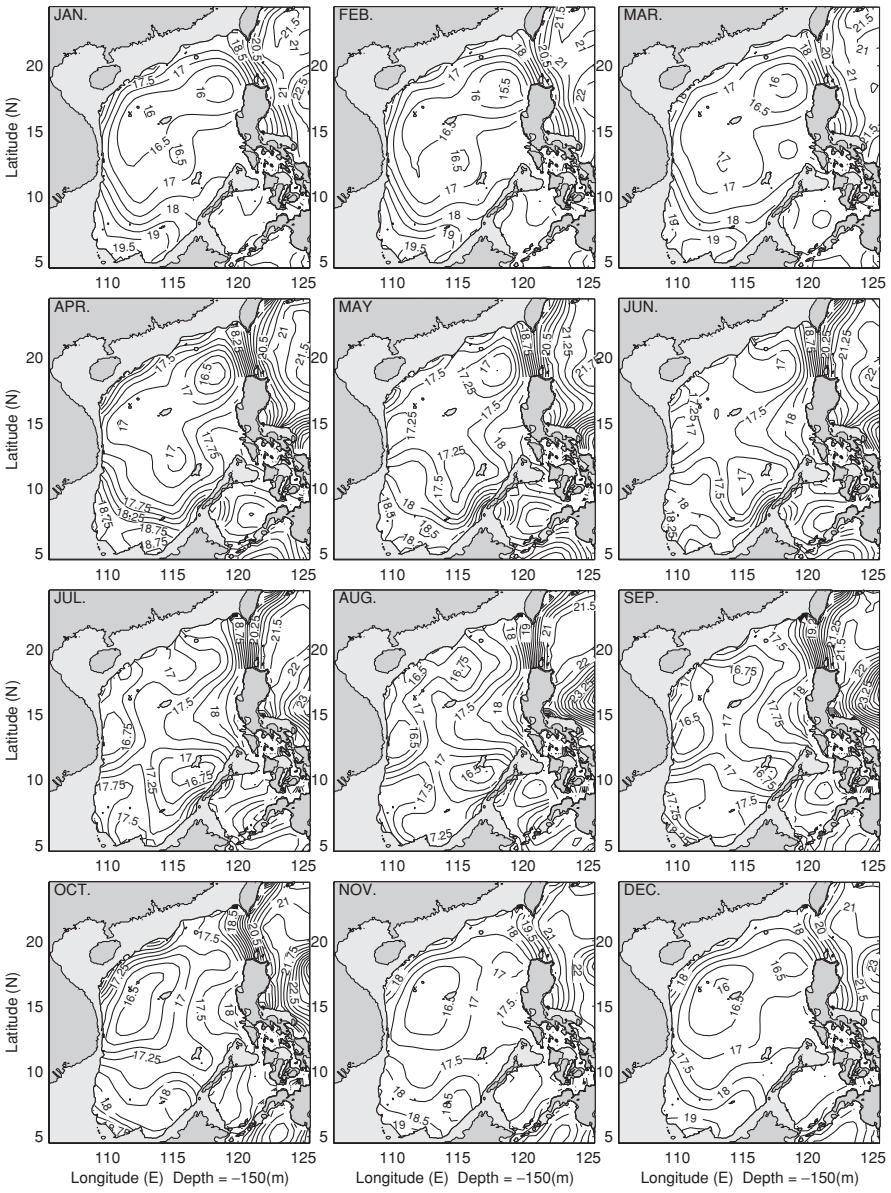

Fig. 6.28. Monthly mean temperature (°C) fields at 150-m depth obtained from GDEM (from Chu and Li 2000, Journal of Physical Oceanography)

Luzon and south of Dongsha, near Vietnamese Bight, Xisha, and Liyue Bank. Dale (1956) and Uda and Nakao (1972) reported a cold eddy off the central Vietnam Bight in summer. Nitani (1970) found a cold eddy located northwest

of Luzon in summer. These two cold centers occurring in summer were also simulated by Chao et al. (1996) with the help of a primitive equation model. The warm water appears in the vicinity of the cool water. A transient central warm pool was identified in spring (Chu et al. 1997c,d, 2002c). A warm water mass is situated in the Philippine Sea all the year round, east of the Luzon Strait, where a strong front appears between the warm Kuroshio water and cool South China Sea water. Other two warm centers appear southwest of Luzon, and northwest of Borneo.

The South China Sea seasonal thermal variability can be characterized by strengthening/weakening of the major cool pool. The basin-wide cool pool expands during winter and shrinks during summer. In December, this cool pool occupies the vast area of the South China Sea from 9°N to 20°N with two evident cold centers: the Northwest Luzon cold center (located at 116°–120°E, 16° 19°N) strengthens during the winter monsoon season and however, the Xisha cold center weakens and disappears in February and March. On the other hand, the cold center near the Vietnamese Bight (located at 109°–112°E, 12°–16°N) appears in May and strengthens during the summer monsoon season and, however, at the same time the Northwest Luzon cold center weakens and disappears.

The warm tongue penetrates northwestward right after passing through the Luzon Strait from Kuroshio and then stretches southwestward along the western boundary of the South China Sea with a very narrow width (100–200 km). This is consistent with other research on climatological data (Shaw 1989; 1991) and historical observational data (Li et al. 1998; Qu et al. 2000; Liu et al. 2001).

The Southwest Luzon warm center (located at 116°–120°E, 12°–14°N) occurs in March. The warm tongue associated with this warm center expands westward during the spring-to-summer transition, and occupies the east part of central South China Sea basin in the summer monsoon season (June–September). During the autumn-to-winter transition (October–November) the Xisha cold center occurs and strengthens in December.

6.6.4 Monthly Mean Salinity Field

Figure 6.29 is the horizontal depiction of monthly mean salinity at 150 m depth. The contour interval is 0.05 ppt. The most evident feature is the advance/retreat of the salty tongue represented by 34.60 ppt isoline from the Philippine Sea through Luzon Strait. This salty tongue penetrates northwestward right after passing through the Luzon Strait and then stretches southwestward along the western boundary of the South China Sea. The salty tongue has the minimum penetration into the South China Sea in October. As the salt tongue advances into the northwestern South China Sea along the Chinese–Vietnamese coast, a salty center occurs near Dongsha (115°–117°E, 19°–21°N) in December. As the salty tongue further advances for the next six months (January–June), the Dongsha salty center weakens

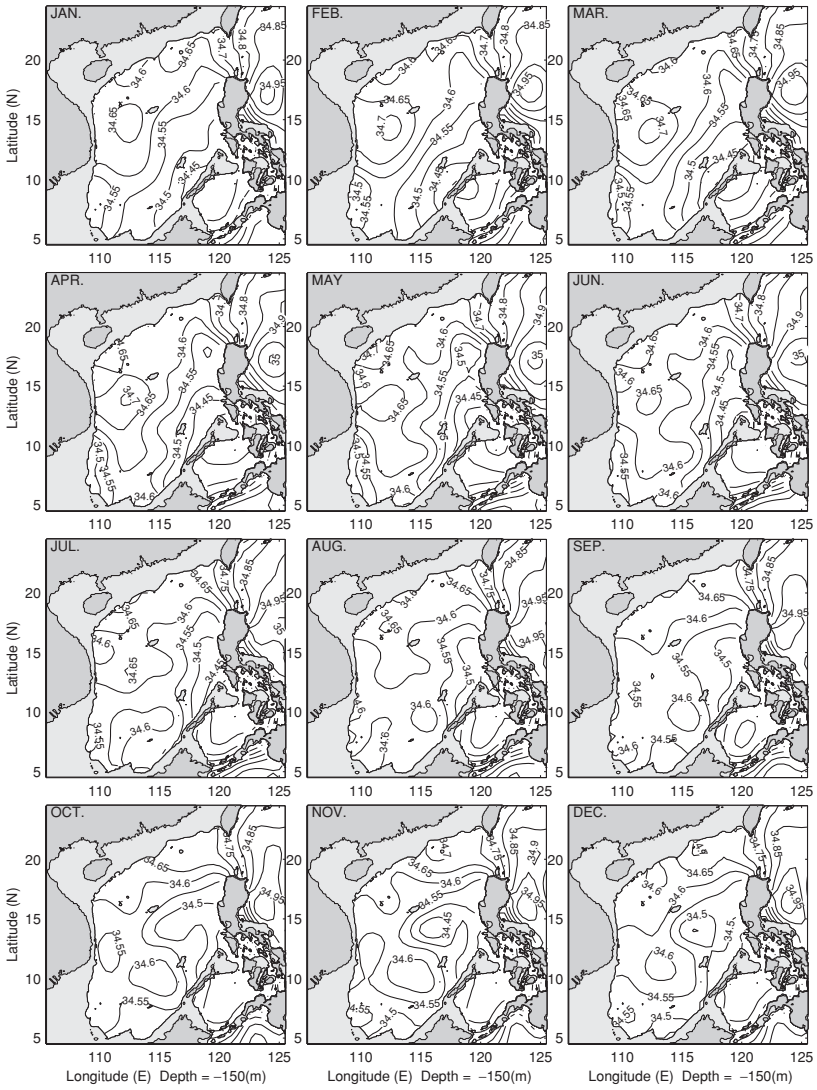

Fig. 6.29. Monthly mean salinity (ppt) fields at 150-m depth obtained from GDEM (from Chu and Li 2000, Journal of Physical Oceanography)

and disappears in March, and an evident salty center shows up near the Vietnamese Bight (110°–113°E, 14°–16°N) for six months (January–June) with salinity greater than 34.7 ppt in February, March, April, and greater than 34.65 ppt in other months. June is characterized as the maximum penetration of the salty tongue into the South China Sea. The salty tongue starts to retreat in July and the salty center near Vietnamese Bight weakens. A salty center appears in southeastern South China Sea west of Palawan-Borneo

(114°–116°E, 8°–11°N) enclosed by 34.6 ppt. This salty center expands toward the west until December.

Such a feature is to some extent inconsistent with the earlier studies (e.g., Shaw 1991). This is due to the sparse salinity observations in the South China Sea. The MOODS dataset for building the GDEM climatology has lesser salinity than temperature stations. The seasonal variability depicted here is not reliable for certain regions such as the region between Liyue Bank and Nansha, where there is no observational data.

6.6.5 Monthly Mean Pressure Field

We use the formulae described in Sect. 4.3 to transform (T, S) data from z- to isopycnal- coordinate system and (4.25) and (4.26) to calculate the monthly mean pressure filed at the isopycnal surfaces. Let the isopycnal surfaces $\sigma_\theta = 23.0$, and $26.2\,(\mathrm{kg\,m^{-3}})$ represent subsurface, and intermediate-level, respectively. Inhomogeneous pressure distribution on the isopycnal surface indicates upwelling (low pressure) and downwelling (high pressure) of that surface.

(a) *Subsurface* ($\sigma_\theta = 23.0\,\mathrm{kg\,m^{-3}}$). The typical pattern (Fig. 6.30) is the pressure increase from the northwest boundary (Chinese–Vietnamese coast) to the southeast boundary (Luzon–Palawan–Borneo). The isoline of $p = 70$ decibar (db) separates the South China Sea into two parts: northwest low pressure and southeast high pressure regions. The southeast South China Sea (high pressure region) has less seasonal variation than the northwest South China Sea (low pressure region). The southeast high pressure near Luzon–Palawan–Borneo expands northwestward in summer and retreats in winter. The Luzon–Palawan–Borneo high pressure is broken into two centers in June: One is enclosed by 80 db isoline and located at the southwest South China Sea (110°–112° E, 8°–10°N), and the other is near Luzon–Palawan. The southwest South China Sea high pressure center expands northeastward in July and August, and joins the Luzon–Palawan–Borneo high pressure in October.

The seasonal variation of the northwest South China Sea low pressure region is depicted as follows. A small low pressure center with a closed isoline of 50 db occurs near the Vietnamese Bight in September. This low pressure center expands northeastward from October to December, and occupies the northern South China Sea (north of 15°N) until February. From April to August the low pressure ($p \leq 50\,\mathrm{db}$) retreats toward the Chinese–Vietnamese coast accompanying with the northwestward expansion of the Luzon–Palawan–Borneo high pressure. In September, the low pressure region shrinks to a small center near the South Vietnam Bight.

(b) *Intermediate level* ($\sigma_\theta = 26.2\,kg\,m^{-3}$) Seasonal variation of the intermediate level is weaker than the subsurface level. The typical pattern is the existence of a permanent South China Sea basin-scale low pressure with one permanent and two seasonal low pressure centers (Fig. 6.31).

Fig. 6.30. Monthly mean subsurface ($\sigma_\theta = 23.0\,kg\,m^{-3}$) pressure field (unit: db) (from Chu and Li 2000, Journal of Physical Oceanography)

The isoline of $p = 310$ db may be used to separate low and high pressure regions. The permanent low pressure center is located near Dongsha (called the Dongsha Low). Two seasonal low pressure centers are found near Vietnamese Bight from May to September and near Luzon–Palawan in July and August. Note that there exists a strong pressure gradient across the Luzon Strait from higher pressure ($p > 420$ db) in the Philippine Sea to lower pressure in the South China Sea ($p < 340$ db). If Kuroshio intrusion occurs at this level ($\sigma_\theta = 26.2\,\mathrm{kg\,m^{-3}}$) then the intruded Kuroshio water moves upward through Luzon Strait.

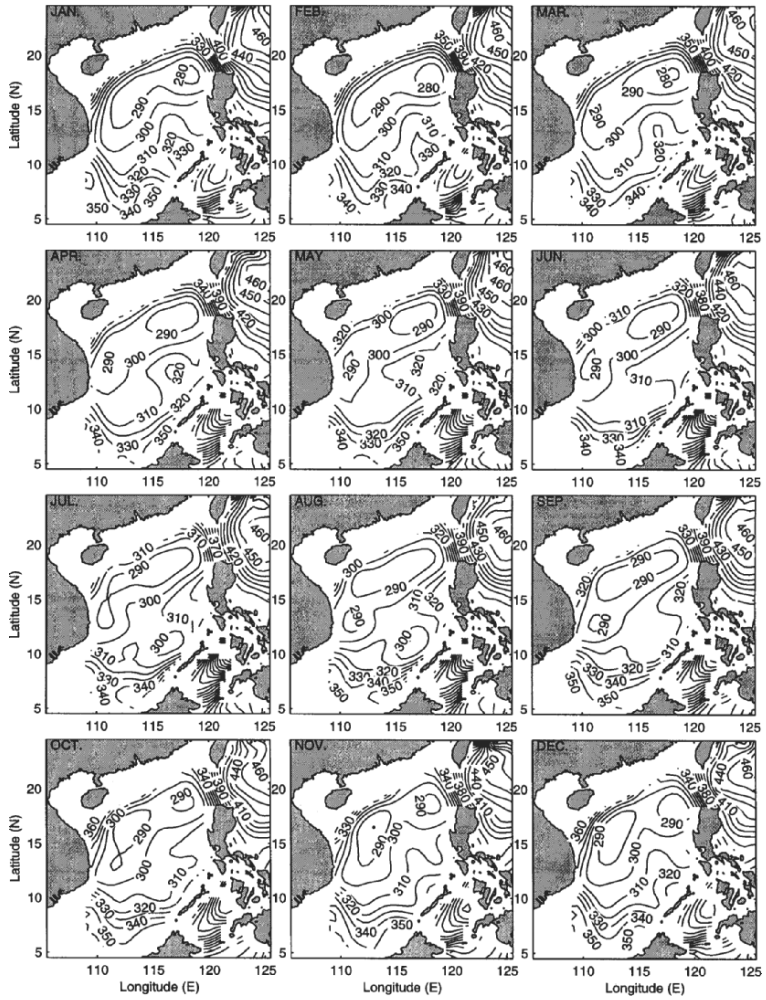

Fig. 6.31. Monthly mean intermediate level ($\sigma_\theta = 26.2\,\mathrm{kg\,m^{-3}}$) pressure field (unit: db) (from Chu and Li 2000, Journal of Physical Oceanography)

6.6.6 Monthly Mean Potential Vorticity Field

Equation (4.28) is used to calculate the potential vorticity at isopycnal surfaces. Inhomogeneous potential vorticity distribution on the isopycnal surface indicates that the P-vector can be determined as the tangential unit vector of the q-isolines.

(a) *Subsurface* ($\sigma_\theta = 23.0\,\mathrm{kg\,m^{-3}}$). Seasonal variation of the potential vorticity is characterized by the domination of a closed high over the South China Sea with the maximum value greater than $1.8 \times 10^{-9}\,\mathrm{m^{-1}, s^{-1}}$ in winter, and the northwestward monotonically increasing of the potential vorticity over the

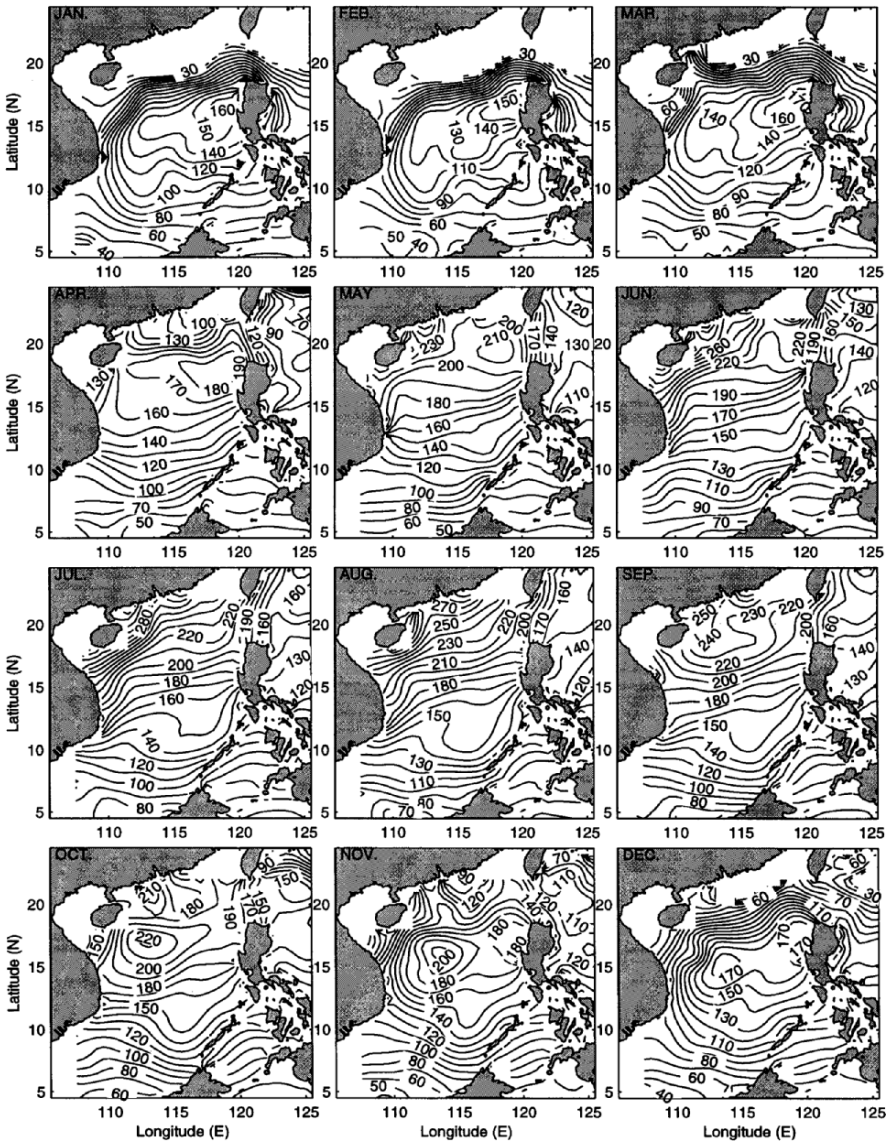

Fig. 6.32. Monthly mean subsurface ($\sigma_\theta = 23.0\,\mathrm{kg\,m^{-3}}$) potential vorticity (unit: $10^{-11}\,\mathrm{m^{-1}\,s^{-1}}$) (from Chu and Li 2000, Journal of Physical Oceanography)

South China Sea basin from the southern boundary in summer. The q-isolines intersect with the Luzon Strait in winter and run parallel to the Luzon Strait in summer (Fig 6.32). Since the geostrophic velocity is along the q-isolines, there is crossing Luzon Strait flow during winter and paralleling Luzon Strait flow during summer. Several authors (Shaw 1989; Chu and Li 2000) discussed

the Kuroshio intrusion into the South China Sea during winter. We may call the winter (summer) q-pattern as the intrusion (nonintrusion) pattern. The evident seasonal variation (intrusion and nonintrusion) on the subsurface may be caused by its shallow depths (Fig. 6.32). As depth increases, the seasonal reversal of the transport across the Luzon Strait weakens. At 150 m depth, the salinity field (Fig. 6.29) does not imply such a seasonal reversal.

The winter intrusion pattern begins in November with a basin-scale high potential vorticity over the South China Sea. This high potential vorticity expands and occupies the whole basin from December to March. Since the Kuroshio water enters the South China Sea through Luzon Strait in winter, it is reasonable to expect a basin-scale cyclonic gyre. In April, the potential vorticity high shrinks and retreats northward. The q-isolines become paralleling to the Luzon Strait. This tendency continues in May and eventually becomes the summer (June–September) nonintrusion q pattern with the disappearance of the basin-scale potential vorticity high. It reoccurs in the northern South China Sea in October with a maximum value greater than $2.2 \times 10^{-9}\,\mathrm{m^{-1}\,s^{-1}}$ near Xisha, and expands southward in November. The winter intrusion q-pattern begins.

(b) *Intermediate level* ($\sigma_\theta = 26.2\,kg\,m^{-3}$). Seasonal variation of potential vorticity at the intermediate level is weaker than at the subsurface level. The seasonal variation (Fig. 6.33) is characterized by strengthening (weakening) of a potential vorticity high over the basin in summer (winter). The basin-scale northeast-to-southwest oriented potential vorticity high is weak in December and January. A small closed high occurs near (114°E, 18°N) with the maximum value greater than $2.5 \times 10^{-10}\,\mathrm{m^{-1}\,s^{-1}}$ in February, and strengthens slowly in spring and the closed potential vorticity high ($2.5 \times 10^{-10}\,\mathrm{m^{-1}\,s^{-1}}$) shifts toward west near Dongsha in May. This Dongsha potential vorticity high center becomes stationary throughout the whole of summer monsoon season (June–September) and the transition season (October–November).

6.6.7 Monthly Mean Circulations

Most important features from the P-vector method are the Kuroshio intrusion, basin gyre, flow separation, and mesoscale eddies. The inverted monthly circulation agrees quite well with earlier observational study (Wyrtki, 1961a, b) at the surface and with modeling results (Chu et al., 1999cd, 2001c) at the deeper levels.

(a) *Subsurface* ($\sigma_\theta = 23.0\,kg\,m^{-3}$). The subsurface shows a strong seasonal variation (Fig. 6.34). Due to the shallowness of the level, $\sigma_\theta = 23.0$, the Kuroshio east of the Luzon Strait is not well inverted. Warm and salty Kuroshio water enters the South China Sea through Luzon Strait evidently in October–March, the transition and during the winter monsoon season. The winter circulation pattern is the basin-wide cyclonic gyre. A cyclonic mesoscale eddy splits from the gyre near Dongsha in February, strengthens afterwards, and becomes evident through the whole of summer monsoon season. The

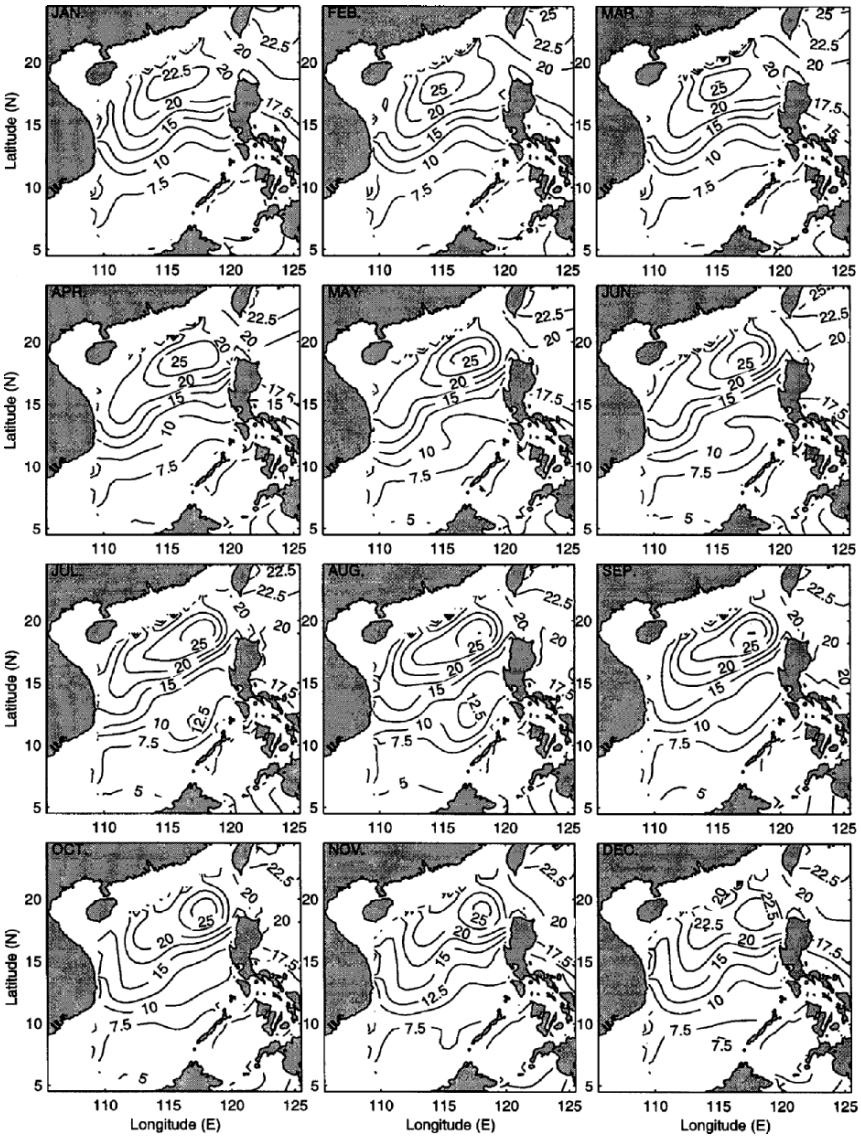

Fig. 6.33. Monthly mean intermediate level ($\sigma_\theta = 26.2\,\mathrm{kg\,m^{-3}}$) potential vorticity (unit: $10^{-11}\,\mathrm{m^{-1}\,s^{-1}}$) (from Chu and Li 2000, Journal of Physical Oceanography)

Kuroshio intruded flow is expected to be confined near the continental slope south of China. The Dongsha cyclonic eddy is undetectable from November to January. On the other hand, the basin-wide cyclonic gyre weakens in April with the disappearance of the southward western boundary currents near the Vietnamese coast.

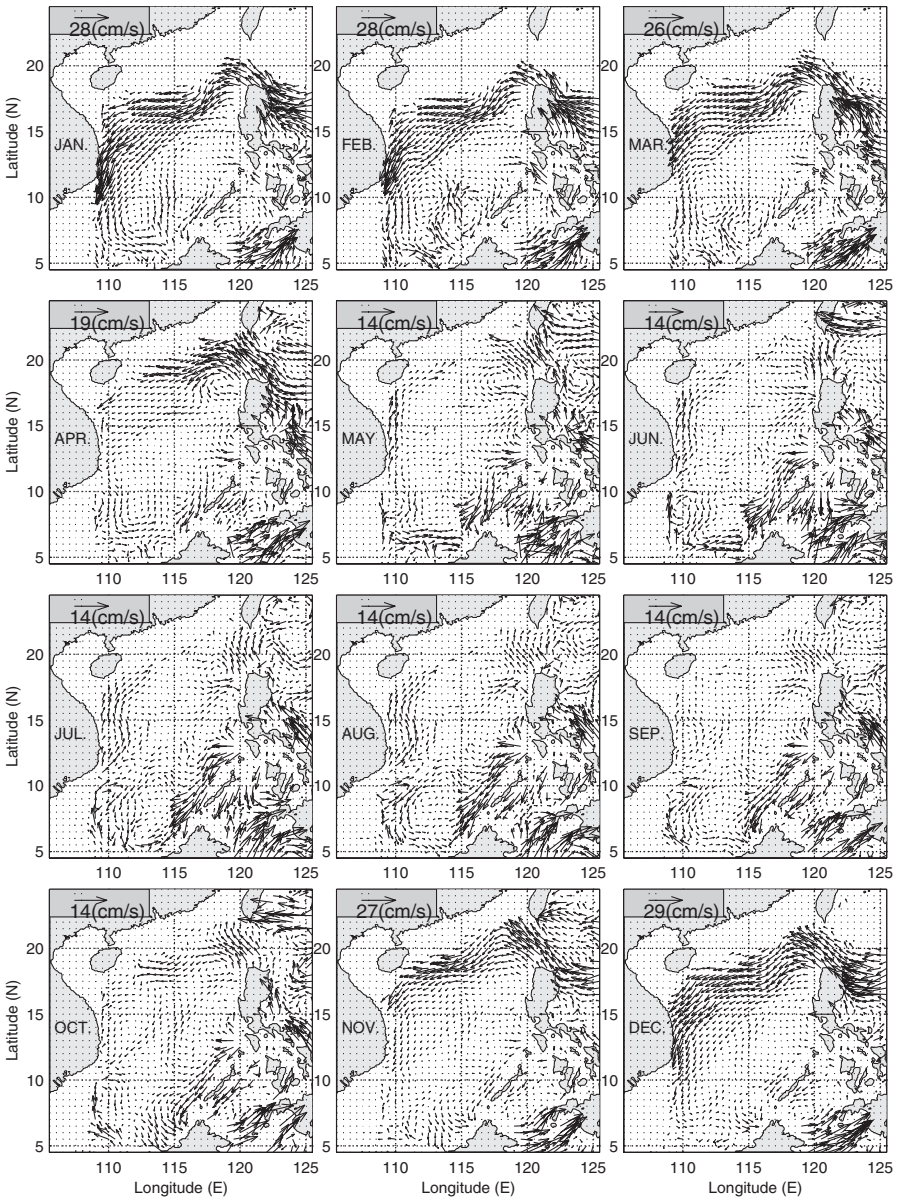

Fig. 6.34. Monthly mean subsurface ($\sigma_\theta = 23.0\,\mathrm{kg\,m^{-3}}$) velocity vector field (from Chu and Li 2000, Journal of Physical Oceanography)

The summer (June–August) pattern is generally a weak anticyclonic gyre. A northward western boundary current occurs from the south to the Vietnamese coast with a weaker speed (less than $0.1\,\mathrm{m\,s^{-1}}$) than its counterpart

(southward western boundary current) in winter. The western boundary current splits into two currents at 10°N: the coastal current and the off-shore current. The off-shore current recirculates and forms a mesoscale anti-cyclonic eddy near Natuna Island. The Natuna eddy was simulated using a numerical model (Chu et al. 1999d). The coastal branch continues north and then east at Hainan Island.

(b) *Intermediate level* ($\sigma_\theta = 26.2\,kg\,m^{-3}$). As the water depth increases, the seasonal variation of the inverted velocity reduces with depth. The intermediate level ($\sigma_\theta = 26.2$), changing from 280 to 460 db, has a persistent basin-scale cyclonic gyre as the major feature of the circulation. There is no seasonal reversal of the western boundary current. The seasonal circulation variability is featured by strengthening, weakening, and splitting of a basin-wide cyclonic gyre (Fig. 6.35). This gyre is evident and strong in winter and weakens in summer. As spring approaches (April–May), the western boundary currents (southward) near the South Vietnam Bight weaken. This "broken" gyre feature continues in the whole of summer (June–August). The western boundary currents (southward) intensify in the Fall. The cyclonic basin-scale gyre all the year round at the intermediate level consists of the numerical models (Metzger and Hurlburt 1996; Chu et al. 1999c, d).

6.6.8 Kuroshio Intrusion Through Luzon Strait

The seasonal variation of the intrusion of the Kuroshio Water into the South China Sea through the Luzon Strait has been investigated in earlier studies (Shaw 1989; 1991). As pointed out by Shaw (1991), the intrusion process is important not only to the transport of water masses into the South China Sea, but also to the shelf circulation off the southeast coast of China. Shaw (1989) used the discriminant-analysis method to classify the water mass T, S characteristics at 150, 200, and 250 m, and found that water characteristics of the Philippine Sea (Kuroshio) were identifiable along the continental margin south of China from October to January. The presence of this water indicated an intrusion current from the Philippine Sea into the South China Sea.

The inverted east–west velocities on the isopycnal surfaces along 120°45′E longitude with the minimum distance between Taiwan and Luzon are used to represent the flow across the Luzon Strait (Fig. 6.36). Positive values show the outflow from the South China Sea to the Philippine Sea, and negative values represent the inflow from the Philippine Sea to the South China Sea (Kuroshio intrusion).

The estimate of the transport through the Luzon Strait is sensitive to the cross-section selection due to larger gradient of the property (temperature, salinity, and Montgomery potential, etc.) in the zonal direction than in the latitudinal direction. The signal of the zonal flow might be contaminated by the fluctuation of the Kuroshio.

The flow through the Luzon Strait has a strong seasonal variation in the upper and intermediate layers. Evident Kuroshio intrusion occurs from

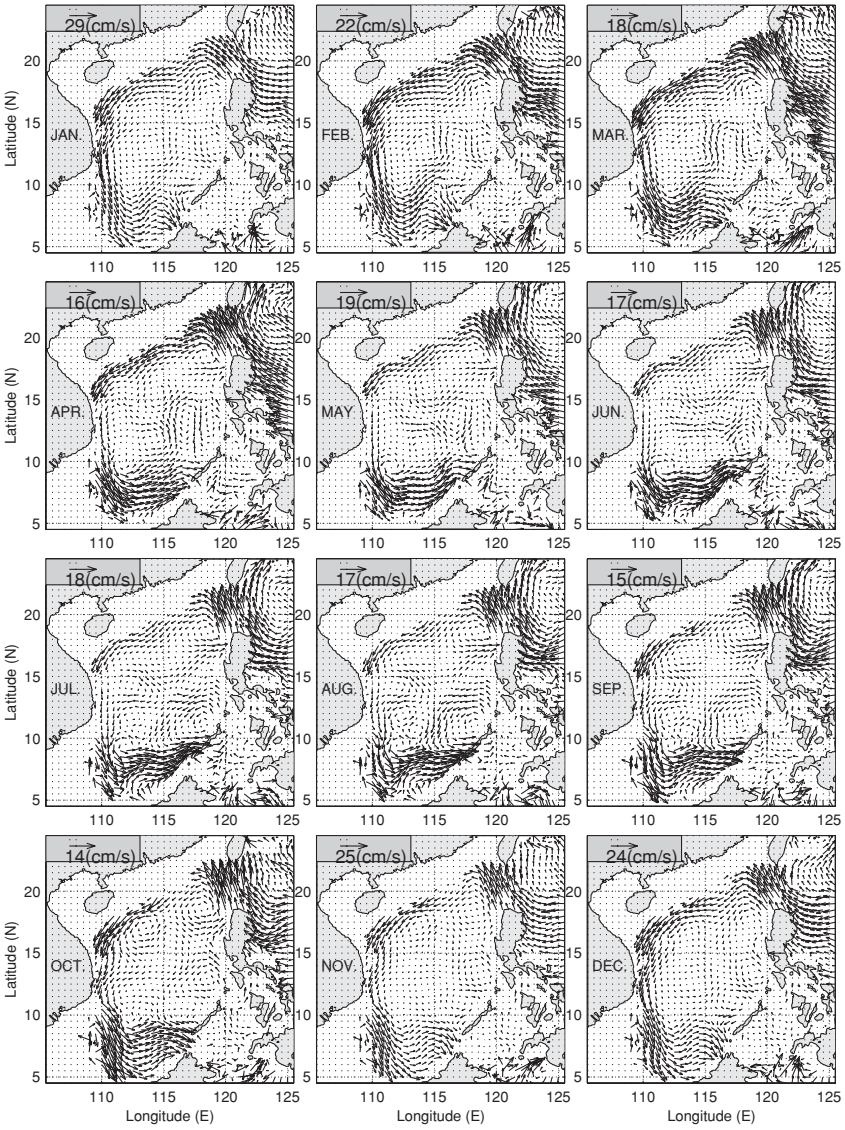

Fig. 6.35. Monthly mean intermediate level ($\sigma_\theta = 26.2\,\mathrm{kg\,m^{-3}}$) velocity vector field (from Chu and Li 2000, Journal of Physical Oceanography)

November to April from the surface to $\sigma_\theta = 27.0$ with the maximum speed of $0.18\,\mathrm{m\,s^{-1}}$ in the middle of the Strait at $\sigma_\theta = 23.75$ in December. From January to March the core of this jet splits into two jet-cores. The upper jet-core ($\sigma_\theta = 24.0$) shifts toward the south (Luzon Island) with the maximum speed reducing from $0.17\,\mathrm{m\,s^{-1}}$ (January) to $0.14\,\mathrm{m\,s^{-1}}$ (March). The lower jet-core

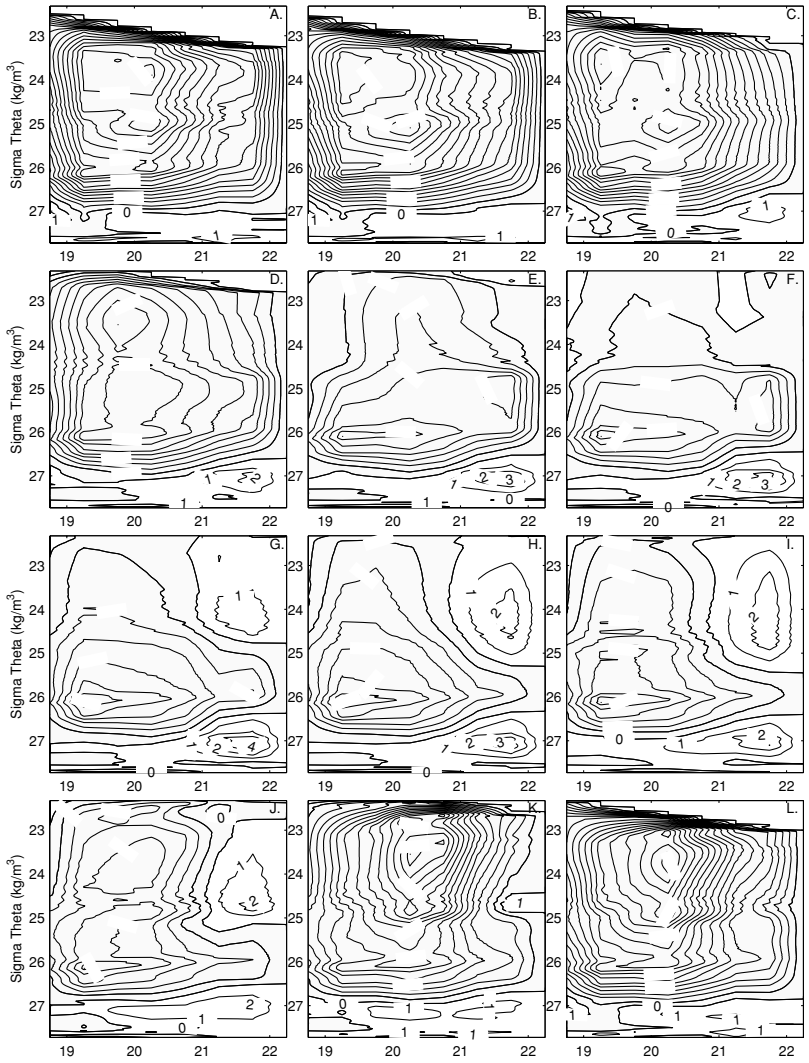

Fig. 6.36. Monthly mean east–west velocities (eastward positive) on the isopycnal surfaces along 120°45′E longitude representing the flow across Luzon Strait (unit: $10^{-2}\,\mathrm{m\,s^{-1}}$) (from Chu and Li 2000, Journal of Physical Oceanography)

($\sigma_\theta = 25.0$) keeps the same location in the middle of the Strait (20°−20°30′ N). In spring and summer, the Kuroshio intrusion weakens drastically. The maximum speed becomes $0.06\,\mathrm{m\,s^{-1}}$ at the intermediate level ($\sigma_\theta = 26.0$) in the southern part of the Luzon Strait (near 19.5°N) from May to October. Weak outflow ($0.02\,\mathrm{m\,s^{-1}}$) to the Philippine Sea occurs in the northern part of the Luzon Strait (north of 20°45′N) from the surface to $\sigma_\theta = 25.5$ during the summer monsoon season.

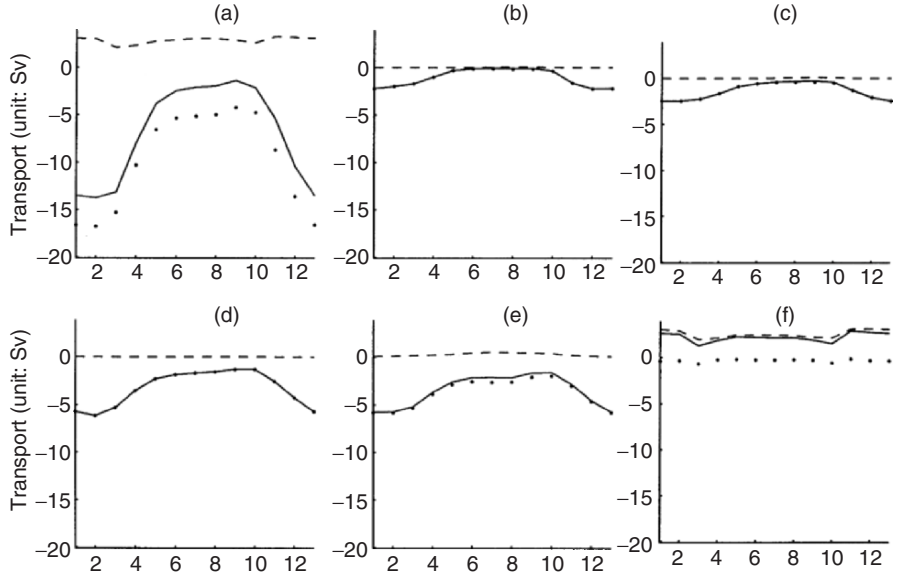

Fig. 6.37. Monthly mean east–west velocity (eastward positive) on the isopycnal surfaces along 120°45′ E longitude representing the flow across the Luzon Strait (unit: $10^{-2}\,\mathrm{m\,s^{-1}}$) (from Chu and Li, 2000, Journal of Physical Oceanography)

Figure 6.37 and Tables 6.3–6.8 show the monthly total and layered (between two σ_θ levels) volume transports through Luzon Strait. The dashed, dotted, and solid curves indicate outflow (eastward), inflow (westward), and net transports. The outflow is much weaker than the inflow for the total transport and the most layered transports except the deep layer ($\sigma_\theta \geq 27.025$), where the outflow is dominant. The total transport is negative (inflow) all year round with a minimum value of −13.7 Sv in February and a maximum value of −1.4 Sv in September with the annual transport of −6.5 Sv, which is between Metzger and Hurlburt's (1996) estimation (2.4 − 4.4 Sv) and Huang et al.'s (1994) estimation (8 − 10 Sv). The total and layered volume transports at the Luzon Strait might be useful for South China Sea numerical modeling.

There is a time-lag in seasonal variations between the Kuroshio intrusion and the salty tongue penetration (Fig. 6.29) at 150-m depth (near $\sigma_\theta = 25.0$): the Kuroshio intrusion (Fig. 6.33) is the strongest in January, and the salty tongue has the maximum penetration in June. Such a lag (4–5 months) is approximately the travel time for the Kuroshio water penetrating from Luzon Strait into the southern South China Sea. For a rough estimation, water particles in winter (December–February) enter the Luzon Strait with a speed around of $0.10\,\mathrm{m\,s^{-1}}$ at 150 m depth and travel 8.64 km each day. The distance between the Luzon Strait and the southern South China Sea is nearly 1,200–1,400 km. It will take approximately 5 months for the water particles traveling from Luzon Strait to the southern South China Seas.

Table 6.3. Monthly variation of the total inflow (westward) and outflow (eastward) volume transport (Sv) at the Luzon Strait (from Chu and Li 2000, Journal of Physical Oceanography)

	Ann	Jan	Feb	Mar	Apr	May	Jun	Jul	Aug	Sep	Oct	Nov	Dec
in	9.35	16.59	16.75	15.25	10.30	6.56	5.36	5.14	4.98	4.23	4.75	8.70	13.61
out	2.85	3.09	3.01	2.10	2.33	2.77	2.90	3.05	3.04	2.86	2.60	3.27	3.20
net (in)	6.50	13.50	13.74	13.15	7.97	3.79	2.46	2.09	1.94	1.37	2.15	5.43	6.50

Table 6.4. Monthly variation of the total inflow (westward) and outflow (eastward) volume transport (Sv) between $\sigma_\theta = 22.20$ and $\sigma_\theta = 24.00$ at the Luzon Strait (from Chu and Li 2000, Journal of Physical Oceanography)

	Ann	Jan	Feb	Mar	Apr	May	Jun	Jul	Aug	Sep	Oct	Nov	Dec
In	0.99	2.20	1.98	1.69	0.97	0.30	0.11	0.10	0.13	0.15	0.35	1.63	2.23
Out	0.02	0.00	0.00	0.00	0.00	0.01	0.02	0.05	0.06	0.08	0.03	0.00	0.00
net (in)	0.97	2.20	1.98	1.69	0.97	0.29	0.09	0.05	0.07	0.07	0.32	1.63	2.23

Table 6.5. Monthly variation of the total inflow (westward) and outflow (eastward) volume transport (Sv) between $\sigma_\theta = 24.00$ and $\sigma_\theta = 25.00$ at the Luzon Strait (from Chu and Li, 2000, Journal of Physical Oceanography)

	Ann	Jan	Feb	mar	Apr	May	Jun	Jul	Aug	Sep	Oct	Nov	Dec
In	1.27	2.46	2.44	2.22	1.62	0.88	0.55	0.41	0.40	0.37	0.47	1.31	2.08
Out	0.03	0.00	0.00	0.00	0.00	0.00	0.01	0.04	0.10	0.13	0.08	0.01	0.00
net (in)	1.24	2.46	2.44	2.22	1.62	0.88	0.54	0.37	0.30	0.24	0.39	1.30	2.08

Table 6.6. Monthly variation of the total inflow (westward) and outflow (eastward) volume transport (Sv) between $\sigma_\theta = 25.00$ and $\sigma_\theta = 26.00$ at the Luzon Strait (from Chu and Li 2000, Journal of Physical Oceanography)

	Ann	Jan	Feb	Mar	Apr	May	Jun	Jul	Aug	Sep	Oct	Nov	Dec
In	3.13	5.71	6.14	5.30	3.53	2.30	1.87	1.69	1.57	1.31	1.31	2.55	4.27
Out	0.00	0.00	0.00	0.00	0.00	0.00	0.00	0.00	0.01	0.03	0.01	0.00	0.00
net (in)	3.13	5.71	6.14	5.30	3.53	2.30	1.87	1.69	1.56	1.28	1.30	2.55	4.27

Table 6.7. Monthly variation of the total inflow (westward) and outflow (eastward) volume transport (Sv) between $\sigma_\theta = 26.00$ and $\sigma_\theta = 27.00$ at the Luzon Strait (from Chu and Li 2000, Journal of Physical Oceanography)

	Ann	Jan	Feb	Mar	Apr	May	Jun	Jul	Aug	Sep	Oct	Nov	Dec
In	3.61	5.80	5.83	5.34	3.91	2.88	2.56	2.63	2.62	2.09	1.98	3.01	4.66
Out	0.27	0.05	0.09	0.14	0.21	0.29	0.42	0.52	0.47	0.43	0.36	0.18	0.09
net (in)	3.34	5.75	5.74	5.20	3.70	2.59	2.14	2.11	2.15	1.66	1.62	2.83	4.57

Table 6.8. Monthly variation of the total inflow (westward) and outflow (eastward) volume transport (Sv) between $\sigma_\theta = 27.00$ and $\sigma_\theta = 27.725$ at the Luzon Strait (from Chu and Li 2000, Journal of Physical Oceanography)

	Ann	Jan	Feb	Mar	Apr	May	Jun	Jul	Aug	Sep	Oct	Nov	Dec
In	0.36	0.41	0.36	0.69	0.26	0.21	0.28	0.31	0.26	0.31	0.63	0.20	0.37
Out	2.53	3.04	2.92	1.95	2.11	2.47	2.46	2.44	2.40	2.20	2.12	3.08	3.10
net (out)	2.17	2.63	2.56	1.26	1.85	2.26	2.18	2.13	2.14	1.89	1.49	2.88	2.73

Questions and Exercises

(1) In determining the parameter γ from two different levels z_k and z_m (or ρ_k and ρ_m), a set of algebraic equations

$$\gamma^{(k)} P_x^{(k)} - \gamma^{(m)} P_x^{(m)} = \Delta u_{km}, \tag{E6.1}$$

$$\gamma^{(k)} P_y^{(k)} - \gamma^{(m)} P_y^{(m)} = \Delta v_{km}. \tag{E6.2}$$

is used. For determining the parameter at k-level,$\boldsymbol{\gamma}^{(k)}$, you may use $(N-1)$ levels $(m = 1, 2, \ldots, k-1, k+1, \ldots, N)$, where N is total number of levels. Prove that the parameter $\boldsymbol{\gamma}^{(k)}$ is the same whichever m-level is used if there is no observational error in the hydrographic data.

(2) If there is observational error in the hydrographic data, do you still get the same value of $\boldsymbol{\gamma}^{(k)}$ using different m-levels? Why?

(3) In the optimization scheme to determine the parameter $\boldsymbol{\gamma}^{(k)}$, a necessary condition (6.16)

$$\begin{vmatrix} A_{11} & A_{12} \\ A_{21} & A_{22} \end{vmatrix} \neq 0,$$

is obtained. Discuss the physical significance of this condition.

(4) In evaluating the P-vector method using MOM, the streamfunction is applied [see (6.24) and (6.25)]. What conditions are assumed? Are they realistic?

(5) What are the major thermal features for the Japan/East Sea from Figs. 6.14 and 6.15?

(6) Discuss the mesoscale thermal characteristics for the Japan/East Sea from Figs. 6.16 to 6.18.

(7) What are the major haline features from Figs. 6.19 and 6.20? Does the salinity show evident features of the Polar Front in the Japan/East Sea?

(8) What are the halocline characteristics in the Japan/East Sea from Figs. 6.21 to 6.23? Discuss these features associated with the Polar Front.

(9) What are the major features of the inverted Japan/East Sea surface current velocities that can be observed from Fig. 6.24? Discuss the current features associated with the thermohaline structure.

(10) Discuss mesoscale eddy features in central Japan/East Sea from Fig. 6.25.
(11) Search the literature to see if the monthly mean volume transport of the Polar Front Current at 135°E shown in Fig. 6.26 is consistent with the earlier results.
(12) Do large stratified lakes and semienclosed marginal seas and estuaries exhibit a persistent cyclonic circulation?
(13) What are the major thermal features for the South China Sea from Fig. 6.28?
(14) What are the major haline features for the South China Sea from Fig. 6.29?
(15) What features can you identify from the isopycnal surface pressure shown in Fig. 6.30 (subsurface) and Fig. 6.31 (intermediate level)? What does strong pressure gradient imply?
(16) What features can you identify from the isopycnal surface potential vorticity shown in Fig. 6.32 (subsurface) and Fig. 6.33 (intermediate level)? Does the water parcel move along the isoline of the potential vorticity? Why?
(17) What are the major features for the South China Sea circulations obtained from Fig 6.32 (subsurface) and Fig. 6.33 (intermediate level)? What are the major differences of the circulations at the two different levels?
(18) Does Fig. 6.36 show evidence of Kuroshio intrusion? In conjunction with Figs. 6.34 and 6.35, discuss the path of the Kuroshio Water in the South China Sea.
(19) Search the literature to find agreement and disagreement of the Kuroshio intrusion into the South China Sea obtained from Fig. 6.36 with the estimation from other authors.